

UNIVERSITY OF CALIFORNIA
RIVERSIDE

Electronic Properties Modeling of Two-Dimensional Materials

A Dissertation submitted in partial satisfaction
of the requirements for the degree of

Doctor of Philosophy

in

Physics

by

Kuan Zhou

December 2018

Dissertation Committee:

Dr. Roger K. Lake, Chairperson
Dr. Shan-Wen Tsai
Dr. Nathaniel Gabor

Copyright by
Kuan Zhou
2018

The Dissertation of Kuan Zhou is approved:

Committee Chairperson

University of California, Riverside

Acknowledgments

Here, I would like to thank my advisor, Prof. Roger K. Lake for giving me the opportunity to join the Laboratory for Terascale and Terahertz Electronics (LATTE) and work with him, for teaching me about device modeling, and for all the support during my PhD. Moreover, as a graduate student, I am always inspired by his attitude towards research and details. Without his constant help, this work would not be possible. I acknowledge support and guidance from Prof. Jeanie Lau for allowing me to collaborate with their respective groups, valuable discussions on our collaborative research projects.

I am grateful for the opportunity I had to collaborate and discuss research with Dr. Darshana Wickramaratne, Dr. Supeng Ge, Dr. Yanmeng Shi, Dr. Yafis Barlas, Dr. Amrit De, Dr. Gen Yin, Dr. Shanshan Su and Dr. Yizhou Liu . A special thanks to the members of LATTE lab for their advice, support and many informal discussions during my PhD.

On the personal side, I would like to acknowledge my friends and family for their continuous support. To my parents, Junyang Zhou and Hongxia Yuan, I am thankful for their guidance and support of my education throughout all these years.

The text of this dissertation, in part or in full, is a reprint of the material as it appears in the following journals:

- Physical Chemistry Chemical Physics [1]. Reprinted with permission from [1]. ©[2017].
Royal Society of Chemistry
- Physical Review Letters [2]. Reprinted with permission from [2]. ©[2018]. American
Physical Society

The co-author Roger K. Lake, listed in the publication directed and supervised the research which forms the basis for this dissertation. The remaining co-authors listed provided technical expertise and support as collaborators. This work is supported in part by FAME, one of six centers of STARnet, a Semiconductor Research Corporation program sponsored by MARCO and DARPA and the NSF EFRI-1433395. This work used the Extreme Science and Engineering Discovery Environment (XSEDE), which is supported by National Science Foundation grant number ACI-1053575.

To my parents for all the support.

ABSTRACT OF THE DISSERTATION

Electronic Properties Modeling of Two-Dimensional Materials

by

Kuan Zhou

Doctor of Philosophy, Graduate Program in Physics
University of California, Riverside, December 2018
Dr. Roger K. Lake, Chairperson

Two-dimensional materials including graphene and transition metal dichalcogenides semiconductors are of tremendous interest for potential electronic applications because of their electronic properties and rich physics. In this work, using tight binding models, first principle calculation and non equilibrium Green's function(NEGF) simulations, interlayer resistance of misoriented MoS₂, electronic properties of tetralayer graphene and edge states of trilayer graphene nanoribbons are successively studied.

In transition metal dichalcogenides like MoS₂, interlayer misorientation alters the interlayer distance, the electronic bandstructure, and the vibrational modes, but, its effect on the interlayer resistance is not known. We analyze the coherent interlayer resistance of misoriented 2H-MoS₂ for low energy electrons and holes as a function of the misorientation angle. The electronic interlayer resistance monotonically increases with the supercell lattice constant by several orders of magnitude similar to that of misoriented bilayer graphene. The large hole coupling gives low interlayer hole resistance that weakly depends on the misorientation angle. Interlayer rotation between an n-type region and a p-type region

will suppress the electron current with little effect on the hole current. We also estimate numerical bounds and explain the results in terms of the orbital composition of the bands at high symmetry points. Density functional theory calculations provide the interlayer coupling used in both a tunneling Hamiltonian and a non-equilibrium Green function calculation of the resistivity.

In multilayer graphene, as the Fermi level and band structure are readily tunable, they constitute an ideal platform for exploring the Lifshitz transition, a change in the topology of a material's Fermi surface. In tetralayer graphene that hosts two intersecting massive Dirac bands, we provide numerical analysis of multiple Lifshitz transitions and multiband transport, which is manifest as a nonmonotonic dependence of conductivity on the charge density n and out-of-plane electric field D , anomalous quantum Hall sequences and Landau level crossings that evolve with n , D , and B .

Lastly, due to mirror symmetry the bands of ABA stacked trilayer graphene can be identified by their parity with respect to mirror symmetry. The even parity bands exhibit gapped bilayer graphene-like dispersion, while the odd parity bands exhibit a gapped graphene-like dispersion. Using a tight binding model with Slonczewski-Weiss-McClure parameters, we look at the edge states in trilayer graphene nanoribbons in the quantum hall regime. When mirror symmetry is preserved, the system exhibits quantized longitudinal conductance at charge neutrality point, due to counterpropagating even and odd parity edge modes. We study the effects of perpendicular electric field and magnetic field and mirror symmetry breaking disorder on the band structures and longitudinal conductance.

Contents

List of Figures	xi
List of Tables	xiii
1 Motivation	1
1.1 Background and objective	1
1.2 Layout	2
2 Theoretical Methods	4
2.1 Basics of density functional theory	4
2.2 Tight binding model of multilayer graphene	6
2.2.1 Parameter settings	7
2.2.2 Tetralayer graphene	8
2.2.3 Trilayer graphene nanoribbon in electric and magnetic field	9
2.3 Basics of transport calculation	11
2.3.1 Standard 2D-2D tunneling formula	12
2.3.2 Low energy non-equilibrium Green function	13
2.3.3 Boltzmann transport theory	14
3 Interlayer Resistance of Misoriented MoS₂	15
3.1 Introduction	15
3.2 Theoretical Methods	16
3.3 Results and Discussion	23
4 Modeling of Tunable Lifshitz Transitions and Multiband Transport in Tetralayer Graphene	29
4.1 Introduction	29
4.2 Transport properties	30
4.3 Band structures with topology analysis	32
5 Edge States in Trilayer Graphene Nanoribbons	37
5.1 Introduction	37
5.2 Tight banding calculations	39

5.3 Results and Discussion	41
6 Conclusions	45
Appendices	47
A DFT calculation for misoriented MoS ₂	47
B Codes and scripts for modeling	49
Bibliography	57

List of Figures

2.1	Schematic view of the lattice structure of the ABA-stacked trilayer graphene (left) and values of corresponding tight-binding parameters[3].	7
2.2	Rectangular unit cell figuration for tight binding calculation of trilayer nanoribbons.	10
2.3	Demonstration of different elements of the tight binding Hamiltonian. . . .	11
3.1	(a) Atomistic geometry of the 21.78° rotated interface. The semi-transparent arrow indicates the direction of current flow. (b) Reduction to a tight binding chain model for a given valley and \mathbf{k} . The two sites 0 and 1 correspond to the two layers. (c) Commensurate unit cells corresponding to the commensurate misorientation angles.	16
3.2	DFT calculated band structures of (a) unrotated bilayer and (b) 21.78° mis-oriented bilayer MoS ₂ in the absence of SOC. The splittings of the bands due to interlayer coupling are shown in the insets at the K points, and directly on the plots at the Γ points. The interlayer coupling parameters $t'_{\perp}(\mathbf{k})$ are extracted from the DFT calculations of the bilayer electronic bandstructures in the absence of spin orbit coupling.	19
3.3	(a) Interlayer coupling t_{\perp} (meV) of the conduction band valleys at K and Σ labeled K_c and Σ_c , and the valence band valleys at K and Γ labeled K_v and Γ_v . (b) Interlayer resistivity ($\Omega \cdot \mu\text{m}^2$) at the conduction (K_c) and valence (Γ_v) band edges. Both the resistivity and the coupling are plotted versus the commensurate unit cell lattice constant in units of the unrotated lattice constant a_0 . The corresponding angles are shown on the upper horizontal axis. Numerical values for the data are given next to the data points. . . .	20
3.4	A vertical pnp BJT with the emitter rotated with respect to the base. The flow of electrons and holes are shown along with their interface resistances, R_{int}^n and R_{int}^p . The pnp circuit symbol is shown at right.	28

4.1	(a) Longitudinal resistance map $R(n, D)$ in log scale at $B = 0$. The unit is $k\Omega$. (b) Line trace $R(D)$ at the CNP. (c)(d) Line traces $R(n)$ at $D = 0$ (c), -200 [(d), red] and -125 (d, blue) mV/nm, respectively. The traces are offset by $0.2k\Omega$ for clarity in (d). The black arrows indicate the peaks and the CNP. (e) Differentiated simulated $dR/dn(n, D)$ using Boltzman transport theory at the same charge density as (a).	31
4.2	(a)(b) Calculated 3D band structure and its 2D projection $E(k_x)$ at $\Delta = 0$, respectively. In (b), the inset displays the overlap of conduction and valance bands at the CNP. Horizontal dashed lines indicate the energy levels corresponding to the Lifshitz transition points. The red solid and dotted lines are calculated by taking the full Hamiltonian and neglecting the off-diagonal block in the Hamiltonian, respectively. (c) A series of cross sections of band structure showing evolution of the Fermi surfaces by tuning Fermi energy at $\Delta = 0$. (d)(e) Calculated 3D band structure and 2D projection $E(k_x)$ at $\Delta = 25mV$. A band gap at the CNP is opened, and the accidental degeneracy at the intersecting point between two BLG-like bands is broken. The dashed black lines in (e) indicate the energy levels corresponding to the Lifshitz transition points. (f) Evolution of Fermi surfaces at $\Delta = 25mV$ as a function of Fermi energy.	34
5.1	(a) Schematics of hBN-encapsulated TLG device. (b) Phase diagram $\sigma_{xx}(E_{\perp}, B_{\perp})$ at the CNP and $T = 260mK$. The different electronic phases are labeled I through IV	38
5.2	Bands of trilayer graphene decoupled into monolayer-like(red) and bilayer-like(blue) bands.	41
5.3	Bands of zigzag edge trilayer graphene nanoribbon with and without external electric field E_{\perp}	42
5.4	Changes of bands of zigzag edge trilayer graphene nanoribbon in dependence of electric field E_{\perp} and magnetic field B_{\perp}	43

List of Tables

S1	Interlayer distance (d), supercell lattice constant a , indirect energy gap $E_{\Gamma-K}$, and direct gap E_{K-K} as a function of rotation angle.	48
----	--	----

Chapter 1

Motivation

1.1 Background and objective

Moore's law proved accurate for several decades, and has been used in the semiconductor industry to guide long-term planning and to set targets for research and development. However, recently the down-scaling of metal oxide semiconductor (MOS) field effect transistors (MOSFETs) has become limited by short channel effects. Two-dimensional materials including graphene and transition metal dichalcogenides (TMDs) have become one of the most promising materials as next generation semiconductors [4].

Besides the high electron mobility and exceptional mechanical properties, one of the most interesting aspects of graphene is that its low energy excitations are massless, chiral Dirac fermions, which can lead to an anomalous integer quantum Hall effect (IQHE) if subjected to magnetic fields [5] and many other interesting electronic properties [6]. Monolayer and bilayer graphene have weak spin-orbit coupling and do not exhibit a significant band gap. Much research has focused on band structure engineering in multilayer graphene

systems [7, 8]. The band structure of two-dimensional materials are readily tunable, and the electronic properties of multilayer graphene are quite exciting to explore.

Because of the significant band gap and spin orbit coupling, two dimensional transition metal dichalcogenides(TMDs) such as MoS_2 have gained enormous attention [9]. Multilayer and heterostructure stacks of transition metal dichalcogenides exhibit strong spin orbit coupling and non-trivial topology [10, 11, 12], large Seebeck coefficients [13], tunable bandstructure [14, 15], many possibilities for band engineering [16], type II band alignments [17, 18, 19], and rectifying pn junctions [17, 19, 20]. For TMD misoriented bilayers, both experiments and simulations show that the interlayer coupling and the interlayer distance are sensitive to the rotation angle, and that the sensitivity of the coupling is very different for different valleys. Thus it is crucial to explore the effect of misorientation on the interlayer resistivity of TMDs.

Thus the objective of the work here is to provide insights into the electronic properties of two dimensional materials including misoriented MoS_2 and multilayer graphene, and guidelines for future experiments.

1.2 Layout

The research is focused on two specific types of materials: multilayer graphene and misoriented MoS_2 . The topics include band structure, orbital analysis, landau levels, topology analysis and transport calculations. Chapter 2 presents the theoretical methods and models, such as the tight binding model, the basics of density functional theory(DFT), and transport calculations. In Chapter 3, first principle calculations, orbital analysis and

transport calculations are used to study the dependence of interlayer resistance on rotation angles of misoriented MoS₂; In Chapter 4, tight binding models, Landau level calculations and Boltzmann transport theory are used to study the tunable Lifshitz transitions and multiband transport in tetralayer graphene; In Chapter 5, a tight binding model with electric field and magnetic field is used to analyze the properties of edge states of trilayer graphene nanoribbons and counterpropagating quantum mirror hall states . Finally, in Chapter 6 we summarize the key findings of these work.

Chapter 2

Theoretical Methods

This chapter introduces basics of the theoretical methods used in this dissertation including density functional theory(DFT), tight binding models and transport calculations.

2.1 Basics of density functional theory

Density functional theory has long been the mainstay of electronic structure calculations in solid-state physics. This is because approximate functionals were shown to provide a useful balance between accuracy and computational cost. DFT is not just another way of solving the Schrodinger equation. Nor is it simply a method of parametrizing empirical results. Density functional theory is a completely different, formally rigorous, way of approaching any interacting problem, by mapping it exactly to a much easier-to-solve non-interacting problem [21].

To start with, consider a complex system of electrons and nuclei, the Hamiltonian will be:

$$H = T + V_{ext} + V_{int} + E_{nn} \quad (2.1)$$

where T is the electronic kinetic energy, V_{ext} is the potential due to the electron-nuclei interactions, V_{int} is the potential due to electron-electron interactions and E_{nn} is the interaction between nuclei. In DFT, the many-electron wavefunction problem could be approximated and solved in practice. The first Hohenberg-Kohn theorem proves that the ground-state of a many-electron system can be uniquely determined by the electron density of the system. The second Hohenberg-Kohn theory states that the total ground-state energy of such a many-electron system is a functional of the ground-state electron density [22]. Thus the Hamiltonian can be rewritten as a functional of the density n :

$$E(n) = T(n) + \int d^3r V_{ext}(r)n(r) + E_{int}(n) + E_{nn} \quad (2.2)$$

where $T(n)$ is the kinetic energy, V_{ext} is the potential acting on the electrons from the nuclei, $E_{int}(n)$ is the interaction energy of electrons and E_{nn} is the interaction between nuclei.

To further make the many-electron problem trackable, the Kohn-Sham approach replaces the many-body electron wave function with a non-interacting system in an effective potential that has a ground state density that is identical to that of the many body interacting system [23]. The effective Hamiltonian of the non-interacting particles in the Kohn-Sham becomes:

$$V_{KS}(r) = V_{ext}(r) + V_H(r) + V_{XC}(r) \quad (2.3)$$

where V_{ext} is the external potential acting on the electrons due to the nuclei defined as:

$$V_{ext}(r) = \sum_n \frac{-Z_n e}{|r_n - r_e|} \quad (2.4)$$

where Z_n is the nuclear charge and r_n is the position of the nuclei. $V_H(r)$ is the Hartree potential given by:

$$V_H(r) = \int \frac{\rho(r)}{|r - r_e|} dr \quad (2.5)$$

$V_{XC}(r)$ is the exchange-correlation potential which includes electron-electron interactions not included in the Hartree potential.

Two common approaches to approximate the exchange correlation potential include the Local Density Approximation (LDA) and the Generalized Gradient Approximation (GGA). The main rationale behind these approximations is that for electron densities within a solid, exchange and correlation effects occur on a short length scale. Hence, LDA and GGA approximations of DFT accurately describe the properties of materials that resemble a homogeneous electron gas.

2.2 Tight binding model of multilayer graphene

Graphene is made out of carbon atoms arranged in hexagonal structure. The structure can be seen as a triangular lattice with a basis of two atoms per unit cell. There are already many excellent articles covering tight binding modeling of monolayer and bilayer graphene [6]. Here we focus on tight binding model of multilayer graphene systems including tetralayer graphene and trilayer graphene nanoribbons.

2.2.1 Parameter settings

In order to describe the bands of multilayer graphene, we adopt the standard Slonczewski-Weiss-McClure parametrization of the tight-binding model [3, 24].

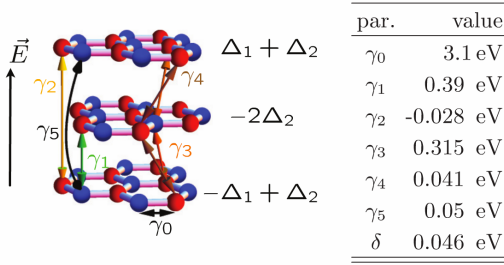


Figure 2.1: Schematic view of the lattice structure of the ABA-stacked trilayer graphene (left) and values of corresponding tight-binding parameters[3].

Take trilayer graphene as an example, six tight-binding parameters $\gamma_0 \dots \gamma_5$ describe hopping matrix elements between different atoms:

$$\begin{aligned}
 A_i &\leftrightarrow B_i : \gamma_0, \\
 B_{1,3} &\leftrightarrow A_2 : \gamma_1, \\
 A_1 &\leftrightarrow A_3 : \frac{1}{2}\gamma_2, \\
 A_{1,3} &\leftrightarrow B_2 : \gamma_3, \\
 A_{1,3} &\leftrightarrow A_2 : -\gamma_4, \\
 B_{1,3} &\leftrightarrow B_2 : -\gamma_4, \\
 B_1 &\leftrightarrow B_3 : \frac{1}{2}\gamma_5,
 \end{aligned} \tag{2.6}$$

where $A_i(B_i)$ refers to an atom from the $A(B)$ sublattice, and index $i = 1 \dots 3$ labels different layers. In addition, parameter δ accounts for an extra on-site potential for B_1 , A_2 , and

B_3 sites, which are on top of each other. Moreover, parameter Δ_1 is responsible for the potential difference between top and bottom layers which is caused by the application of the displacement field to the sample. Parameter Δ_2 describes the deviation of potential on the middle layer from the mean of the potentials on the top and bottom layers.

2.2.2 Tetralayer graphene

In ABAB stacked tetralayer graphene, the Hamiltonian in the vicinity of the K_ξ valley is:

$$H = \begin{bmatrix} \frac{eD \cdot d}{2} & v\pi^\dagger & -v_4\pi^\dagger & v_3\pi & \frac{\gamma_2}{2} & 0 & 0 & 0 \\ v\pi & \delta + \frac{eD \cdot d}{2} & \gamma_1 & -v_4\pi^\dagger & 0 & \frac{\gamma_5}{2} & 0 & 0 \\ -v_4\pi & \gamma_1 & \delta + \frac{eD \cdot d}{6} & v\pi^\dagger & -v_4\pi & \gamma_1 & \frac{\gamma_5}{2} & 0 \\ v_3\pi^\dagger & -v_4\pi & v\pi & \frac{eD \cdot d}{6} & v_3\pi^\dagger & -v_4\pi & 0 & \frac{\gamma_2}{2} \\ \frac{\gamma_2}{2} & 0 & -v_4\pi^\dagger & v_3\pi & -\frac{eD \cdot d}{6} & v\pi^\dagger & -v_4\pi^\dagger & v_3\pi \\ 0 & \frac{\gamma_5}{2} & \gamma_1 & -v_4\pi^\dagger & v\pi & \delta - \frac{eD \cdot d}{6} & \gamma_1 & -v_4\pi^\dagger \\ 0 & 0 & \frac{\gamma_5}{2} & 0 & -v_4\pi & \gamma_1 & \delta - \frac{eD \cdot d}{2} & v\pi^\dagger \\ 0 & 0 & 0 & \frac{\gamma_2}{2} & v_3\pi^\dagger & -v_4\pi & v\pi & -\frac{eD \cdot d}{2} \end{bmatrix} \quad (2.7)$$

where the D is the vertical electric field and d is the thickness of tetralayer graphene. And $\xi = \pm 1$ is the valley index and $\pi = \xi p_x + ip_y$ is the momentum operator. Fermi velocity of graphene $v = \frac{\sqrt{3}a\gamma_0}{2\hbar}$, and related velocities $v_3 = \frac{\gamma_3}{\gamma_0}v$, $v_4 = \frac{\gamma_4}{\gamma_0}v$.

For Landau level calculation, a new set of basis will be used with base wave functions:

$$\begin{aligned}
|\phi_1\rangle &= (0, |0\rangle, 0, 0, 0, 0, 0, 0), \\
|\phi_2\rangle &= (0, 0, 0, |0\rangle, 0, 0, 0, 0), \\
|\phi_3\rangle &= \frac{1}{\sqrt{2}}(|n\rangle, |n+1\rangle, 0, 0, 0, 0, 0, 0), \\
|\phi_4\rangle &= \frac{1}{\sqrt{2}}(0, 0, |n\rangle, |n+1\rangle, 0, 0, 0, 0), \\
|\phi_5\rangle &= \frac{1}{\sqrt{2}}(|n\rangle, -|n+1\rangle, 0, 0, 0, 0, 0, 0), \\
|\phi_6\rangle &= \frac{1}{\sqrt{2}}(0, 0, |n\rangle, -|n+1\rangle, 0, 0, 0, 0), \\
|\phi_7\rangle &= \frac{1}{\sqrt{2}}(0, 0, 0, 0, 0, |0\rangle, 0, 0), \\
|\phi_8\rangle &= \frac{1}{\sqrt{2}}(0, 0, 0, 0, 0, 0, 0, |0\rangle), \\
|\phi_9\rangle &= \frac{1}{\sqrt{2}}(0, 0, 0, 0, |n\rangle, |n+1\rangle, 0, 0), \\
|\phi_{10}\rangle &= \frac{1}{\sqrt{2}}(0, 0, 0, 0, 0, 0, |n\rangle, |n+1\rangle), \\
|\phi_{11}\rangle &= \frac{1}{\sqrt{2}}(0, 0, 0, 0, |n\rangle, -|n+1\rangle, 0, 0), \\
|\phi_{12}\rangle &= \frac{1}{\sqrt{2}}(0, 0, 0, 0, 0, 0, |n\rangle, -|n+1\rangle),
\end{aligned} \tag{2.8}$$

The total Hamiltonian in this new basis can be used to calculate bands. Typically, maximum number of Landau levels N considered could be about 50 or changed accordingly.

2.2.3 Trilayer graphene nanoribbon in electric and magnetic field

For tight binding calculation of trilayer graphene nanoribbons, in order to simulate both zigzag and armchair edges in an united framework, a rectangular unit cell with atoms $\{A_1, B_1, A_2, B_2, A_3, B_3, A'_1, B'_1, A'_2, B'_2, A'_3, B'_3\}$ is chosen as shown in the figure.

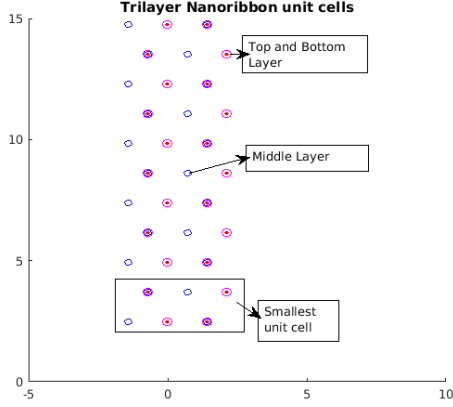


Figure 2.2: Rectangular unit cell figuration for tight binding calculation of trilayer nanoribbons.

In the absence of external electric field, the band structure of the trilayer graphene consists of monolayer-like and bilayer-like bands [25]. And the Hamiltonian can be decoupled to even and odd parity bands in a new basis [3] of

$$\left\{ \frac{A_1 - A_3}{\sqrt{2}}, \frac{B_1 - B_3}{\sqrt{2}}, \frac{A_1 + A_3}{\sqrt{2}}, B_2, A_2, \frac{B_1 + B_3}{\sqrt{2}}, \frac{A'_1 - A'_3}{\sqrt{2}}, \frac{B'_1 - B'_3}{\sqrt{2}}, \frac{A'_1 + A'_3}{\sqrt{2}}, B_2, A_2, \frac{B_1 + B_3}{\sqrt{2}} \right\} \quad (2.9)$$

To calculate the bands, the total Hamiltonian matrix is divided into small parts as $\alpha_u, \beta_0, \beta_1, \beta_2$ and t , which are Hamiltonians of unit cell blocks and interactions between blocks. For different nanoribbon edges, different α (Hamiltonian of supercell) and β (interactions between supercells) are constructed accordingly. In order to decouple even and odd parity bands when no electric field is applied, a transformation matrix M is used to change the basis. Finally, the Hamiltonian is $H(k) = \alpha + \beta' e^{-ka} + \beta e^{ka}$.

With applied perpendicular B-field $(0, 0, B_z)$, a vector potential $(-B_z y, 0, 0)$ or

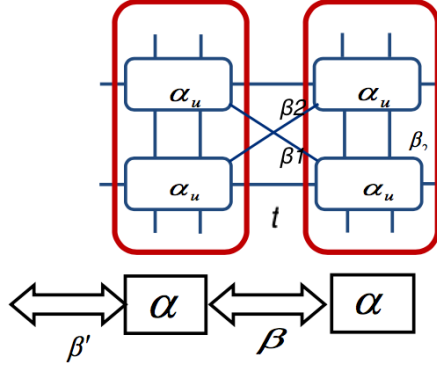


Figure 2.3: Demonstration of different elements of the tight binding Hamiltonian.

$(0, -B_z x, 0)$ is used accordingly based on the edge. The Peierls phase factor and the interactions will be calculated accordingly using:

$$\hat{t}_{ij}^{N-M} \rightarrow \hat{t}_{ij}^{N-M} e^{i\phi_{ij}^{N,M}}$$

where

$$\phi_{ij}^{N,M} = \frac{eB}{2\hbar} (x_i^N - x_j^M)(y_i^N + y_j^M)$$

2.3 Basics of transport calculation

The transport calculation methods covered here include 2D tunneling, low energy non-equilibrium Green function and Boltzmann transport theory. The basics are presented here, and more details will be covered in next chapters.

2.3.1 Standard 2D-2D tunneling formula

In transport calculations for low energies near a given valley minimum, the standard 2D-2D tunneling formula is

$$J = \frac{g_s g_v q}{h \mathcal{A}} \sum_{\mathbf{k}} \int dE |t_{\perp}(\mathbf{k})|^2 A_u(\mathbf{k}; E) A_l(\mathbf{k}; E) \cdot [f(E - E_{f,u}) - f(E - E_{f,l})] \quad (2.10)$$

where $A_u(\mathbf{k}; E)$ is the spectral function of the upper layer, $A_l(\mathbf{k}; E)$ is the spectral function of the lower layer, $t_{\perp}(\mathbf{k})$ is the interlayer coupling which can be determined from the band splitting, $f(E - E_f)$ is the Fermi-Dirac factor, and $E_{f,u(l)}$ is the Fermi level of the upper (lower) layer. In the prefactor, \mathcal{A} is the area, g_s is the spin degeneracy, and g_v is the valley degeneracy. The spectral functions are given by $A_{u(l)} = \frac{\gamma}{(E - \varepsilon(\mathbf{k}))^2 + \frac{\gamma^2}{4}} = \frac{\gamma}{E_z^2 + \frac{\gamma^2}{4}}$ where γ is the lifetime broadening in each layer and in the second equality, we define $E_z \equiv E - \varepsilon(\mathbf{k})$. Since the interlayer coupling t_{\perp} is usually a weak function of \mathbf{k} in van der Waals (Vdw) 2D materials, we could use its value at the band edge. Then, we can perform the sum over the transverse momenta analytically, and Eq. (2.10) now has the form

$$J = \frac{g_s g_v q}{h} \frac{m^*}{2\pi \hbar^2} \int dE_z |t_{\perp}|^2 A_u(E_z) A_l(E_z) \cdot \int_0^{\infty} d\varepsilon [f(E_z + \varepsilon - E_{f,u}) - f(E_z + \varepsilon - E_{f,l})] \quad (2.11)$$

For small voltages, the difference in Fermi factors becomes $\frac{-\partial f}{\partial \varepsilon} qV$ where V is the applied voltage, and the integral over ε gives $f(E_z - E_f) qV$ where E_f is the equilibrium Fermi level. Therefore, the 2D-2D tunneling formula for the interlayer conductivity for low energies is

$$\sigma_{2D} = \frac{g_s g_v q^2}{h} \frac{m^*}{2\pi \hbar^2} \int dE_z \frac{|t_{\perp}|^2 \gamma^2 f(E_z - E_f)}{\left[E_z^2 + \frac{\gamma^2}{4} \right]^2}. \quad (2.12)$$

2.3.2 Low energy non-equilibrium Green function

In transport calculations for strongly coupled bands, a low-energy, 3D-3D transmission model could be used. Physically, this corresponds to a system of two semi-infinite stacks. For each band, at each transverse \mathbf{k} , this model reduces to that of a one dimensional (1D) tight-binding chain. Here we can take misoriented MoS₂ as an example as shown in Fig. 3.1(b). The hopping parameter t_0 is given by t_\perp of the unrotated bilayer. For this model, the ‘device’ consists of the two misoriented layers numbered 0 and 1 in Fig. 3.1(b). The left and right self-energies due to coupling to the semi-infinite leads are $\Sigma^R = t_0 e^{ik_z a}$. The Green function is

$$G^R = \begin{pmatrix} E - \varepsilon_\nu(\mathbf{k}) - t_0 e^{ik_z a} & -t_\perp^\nu(\mathbf{k}) \\ -t_\perp^\nu(\mathbf{k}) & E - \varepsilon_\nu(\mathbf{k}) - t_0 e^{ik_z a} \end{pmatrix}^{-1}. \quad (2.13)$$

The transmission is calculated from $T(E, \mathbf{k}) = \Gamma_u \Gamma_l |G_{0,1}^R(E, \mathbf{k})|^2$ where $\Gamma_l = \Gamma_u = 2|t_0| \sin(k_z a)$.

Using the dispersion relation of the leads, $E = \varepsilon_\nu(\mathbf{k}) + 2t_0 \cos(k_z a)$, this can be analytically evaluated to obtain $T(E_z) = \frac{t_\perp^2 (4t_0^2 - E_z^2)}{(t_0^2 + t_\perp^2)^2 - t_\perp^2 E_z^2}$ where $E_z \equiv E - \varepsilon_\nu(\mathbf{k})$. Going through the same steps as for the 2D-2D tunneling formula, the 3D-3D expression for the conductance is

$$\sigma_{3D} = \frac{g_s g_v q^2}{h} \frac{m^*}{2\pi \hbar^2} \int_{-2t_0}^{2t_0} dE_z \frac{t_\perp^2 (4t_0^2 - E_z^2) f(E_z - E_f)}{(t_0^2 + t_\perp^2)^2 - t_\perp^2 E_z^2}. \quad (2.14)$$

In all calculations of the interlayer conductance, the Fermi level is taken to be $k_B T$ below the conduction band edge when calculating the electron conductance or $k_B T$ above the valence band edge when calculating the hole conductance, with $T = 300\text{K}$.

2.3.3 Boltzmann transport theory

In Boltzmann transport theory, the conductivity can be written as a sum of intra-band and interband contributions [26]:

$$\sigma_{intra}^{xx} = e^2 \tau \sum_n \int_{BZ} \frac{1}{(2\pi)^2} d\theta k dk |\langle n\mathbf{k} | \frac{\partial \mathbf{H}}{\partial \mathbf{k}_x} | n\mathbf{k} \rangle|^2 \left(-\frac{\partial f_{n\mathbf{k}}}{\partial \epsilon_{n\mathbf{k}}} \right) \quad (2.15)$$

$$\sigma_{inter}^{xx} = ie^2 \hbar \sum_{n,m \neq n} \int_{BZ} \frac{1}{(2\pi)^2} d\theta k dk \frac{f_{m\mathbf{k}} - f_{n\mathbf{k}}}{\epsilon_{n\mathbf{k}} - \epsilon_{m\mathbf{k}}} \frac{\langle n\mathbf{k} | \frac{\partial \mathbf{H}}{\partial \mathbf{k}_x} | m\mathbf{k} \rangle \langle m\mathbf{k} | \frac{\partial \mathbf{H}}{\partial \mathbf{k}_x} | n\mathbf{k} \rangle}{\epsilon_{n\mathbf{k}} - \epsilon_{m\mathbf{k}} + i\hbar\tau^{-1}} \quad (2.16)$$

where the ϵ_{nk} and f_{nk} are the energy and Fermi-Dirac distribution function of band n with wave vector k . Usually we can treat the relaxation time τ as an independent parameter and assume that τ is the same for both intraband and interband scattering mechanisms [26].

Chapter 3

Interlayer Resistance of Misoriented MoS₂

3.1 Introduction

For transition metal dichalcogenides(TMD) misoriented bilayers, both experiments and simulations show that the interlayer coupling and the interlayer distance are sensitive to the rotation angle, and that the sensitivity of the coupling is very different for different valleys [27, 28, 29, 30, 31]. A small rotation angle in hetero-bilayers alters the inter-layer exciton dynamics [32, 33]. While the effects of misorientation on the geometry, electronic bandstructure, and vibrational modes of bilayer TMDs have received significant attention, the effect of misorientation on the interlayer resistivity of TMDs has not yet been studied. Recent work considered the effect of misorientation on the in-plane transport [34]. In this work, we theoretically determine the coherent electron and hole interlayer (vertical)

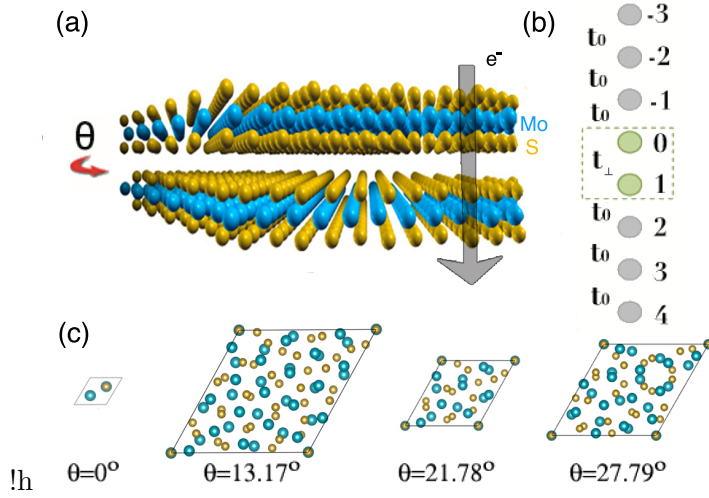


Figure 3.1: (a) Atomistic geometry of the 21.78° rotated interface. The semi-transparent arrow indicates the direction of current flow. (b) Reduction to a tight binding chain model for a given valley and \mathbf{k} . The two sites 0 and 1 correspond to the two layers. (c) Commensurate unit cells corresponding to the commensurate misorientation angles.

conductance of a misoriented MoS₂ interface as illustrated in Fig. 3.1(a).

In MoS₂ bilayers, the low-energy electron transport takes place at the K valley, and the low-energy hole transport takes place at the Γ valley. This results in an extremely asymmetric response of the electron and hole interlayer conductivity to the interlayer misorientation angle. The coherent interlayer electron transport is exponentially suppressed by the misorientation, and the hole transport is only slightly affected.

3.2 Theoretical Methods

The structures considered are a 2H aligned bilayer and misoriented bilayers with commensurate rotation angles. The commensurate unit cells are shown in Fig. 3.1(c), and they are constructed following the method described in Ref. [35]. The rotation angles are $\theta = 13.17^\circ$, 21.78° , and 27.79° , and the corresponding unit cell lattice constants are $\sqrt{19}a_0$,

$\sqrt{7}a_0, \sqrt{13}a_0$ where a_0 is the lattice constant of 2H aligned bilayer equal to 3.16 Å [36].

The purpose of these DFT calculations is to determine the energy splitting of the band edges resulting from the interlayer coupling. The DFT calculations are intentionally performed in the absence of spin-orbit coupling (SOC) to cleanly extract the band splitting from the interlayer coupling [37]. In the absence of SOC, the energy splitting $\Delta_\nu(\mathbf{k})$ of each band ν at wavevector \mathbf{k} due to the interlayer coupling $t_\perp^\nu(\mathbf{k})$ is $\Delta_\nu(\mathbf{k}) = 2|t_\perp^\nu(\mathbf{k})|$. In the basis of the eigenstates of the individual monolayers, the low-energy bilayer Hamiltonian for each band ν is

$$H = \begin{pmatrix} \varepsilon_\nu(\mathbf{k}) & t_\perp^\nu(\mathbf{k}) \\ t_\perp^\nu(\mathbf{k}) & \varepsilon_\nu(\mathbf{k}) \end{pmatrix} \quad (3.1)$$

where $\varepsilon_\nu(\mathbf{k})$ is the low-energy two-dimensional dispersion of band ν .

The interlayer couplings are extracted from the energy splittings near the band edge as illustrated in Fig. 3.2. A semi-log plot of the values versus supercell lattice constant is shown in Fig. 3.3(a). It is clear from Fig. 3.3(a) that the interlayer coupling of the holes at Γ are little affected by the misorientation angle. The interlayer couplings of the electron and hole states at K and Σ are exponentially suppressed as a function of the supercell lattice constant. This exponential dependence of the band splitting on the supercell lattice constant is also found for the band splitting in rotated bilayer graphene [38].

Only the conduction K valley and the valence Γ valley are considered for calculating the low-energy electron and hole interlayer resistances, since HSE level calculations, which provide more accurate values for energy levels, show that the conduction band K valley lies approximately 130 meV below the conduction band Σ valley, and the valence band Γ valley lies 200 meV or more above the valence band K valley. [13, 27, 36, 39]. Once

we restrict our attention to the conduction K valley, which we will denote as K_c , and the valence Γ valley, which we will denote as Γ_v , spin-orbit splitting has little effect on the inter-layer transport, since the spin splitting of the conduction band at K is 1.5 meV and the valence band at Γ is spin degenerate [40]. Since we are interested in the room temperature conductance, we ignore the small spin splitting of the conduction band. To a very good approximation, the low-energy bands within the plane (perpendicular to the transport direction) are parabolic and isotropic [40]. For the transport calculations, we treat them as parabolic using two masses, m_x and m_y , such that $\varepsilon(\mathbf{k}) = \frac{\hbar^2|\mathbf{k}|^2}{2m^*}$ with $m^* = \sqrt{m_x m_y}$. The values for the masses from DFT/HSE calculations for the holes at Γ are $m_x = m_y = 0.62m_0$ and for the electrons at K are $m_x = 0.47m_0$ and $m_y = 0.45m_0$ [41].

After extracting the interlayer coupling elements t_{\perp}^{ν} from the DFT calculations, we calculate the interlayer conductance of the electron and hole bands using two different methods described below. For low energies near a given valley minimum, the standard 2D-2D tunneling formula is

$$J = \frac{g_s g_v q}{h \mathcal{A}} \sum_{\mathbf{k}} \int dE |t_{\perp}(\mathbf{k})|^2 A_u(\mathbf{k}; E) A_l(\mathbf{k}; E) \cdot [f(E - E_{f,u}) - f(E - E_{f,l})] \quad (3.2)$$

where $A_u(\mathbf{k}; E)$ is the spectral function of the upper layer, $A_l(\mathbf{k}; E)$ is the spectral function of the lower layer, $t_{\perp}(\mathbf{k})$ is the interlayer coupling determined from the band splitting, $f(E - E_f)$ is the Fermi-Dirac factor, and $E_{f,u(l)}$ is the Fermi level of the upper (lower) layer. In the prefactor, \mathcal{A} is the area, g_s is the spin degeneracy, and g_v is the valley degeneracy. The standard 2D-2D tunneling formula can be obtained following the derivation leading to

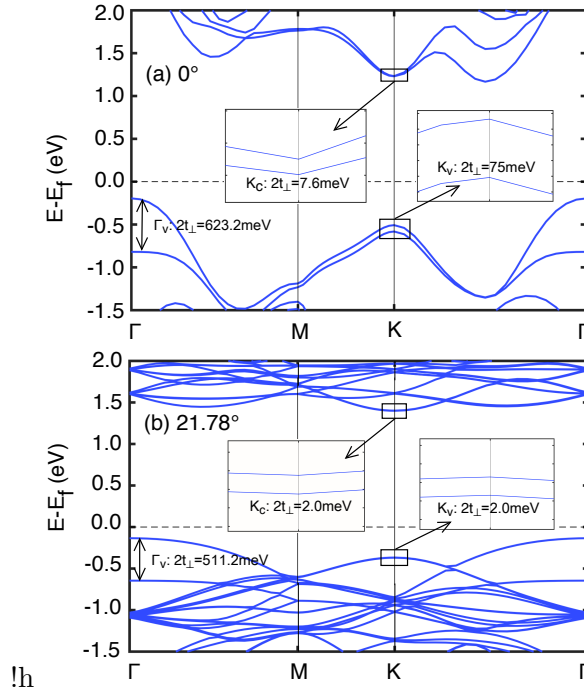


Figure 3.2: DFT calculated band structures of (a) unrotated bilayer and (b) 21.78° mis-oriented bilayer MoS₂ in the absence of SOC. The splittings of the bands due to interlayer coupling are shown in the insets at the K points, and directly on the plots at the Γ points. The interlayer coupling parameters $t''_{\perp}(\mathbf{k})$ are extracted from the DFT calculations of the bilayer electronic bandstructures in the absence of spin orbit coupling.

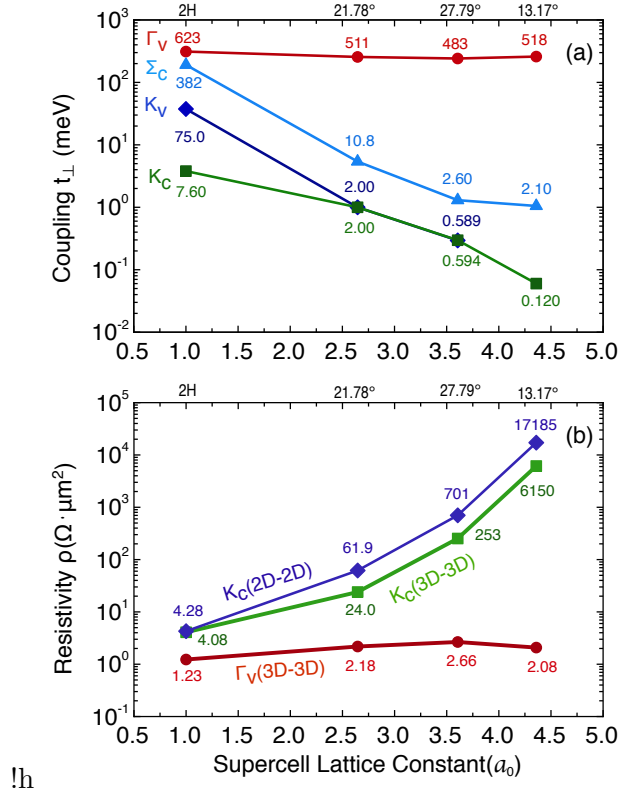


Figure 3.3: (a) Interlayer coupling t_{\perp} (meV) of the conduction band valleys at K and Σ labeled K_c and Σ_c , and the valence band valleys at K and Γ labeled K_v and Γ_v . (b) Interlayer resistivity ($\Omega \cdot \mu\text{m}^2$) at the conduction (K_c) and valence (Γ_v) band edges. Both the resistivity and the coupling are plotted versus the commensurate unit cell lattice constant in units of the unrotated lattice constant a_0 . The corresponding angles are shown on the upper horizontal axis. Numerical values for the data are given next to the data points.

the current expression of Meir and Wingreen [42]

$$J = \frac{g_s g_v q}{hA} \sum_{\vec{k}} \int dE \text{tr} \{ \Gamma_u(E; \mathbf{k}) [f(E - \mu_u) A_l(E; \mathbf{k}) + iG_l^<(E; \mathbf{k})] \}. \quad (3.3)$$

For the system shown in Fig. 1(a) of the main text, A_l and $G_l^<$ are the spectral function and less-than correlation function of the lower layer, and $\Gamma_u(E; \mathbf{k}) = t_{\perp}^2(\mathbf{k}) A_u(\mathbf{k}; E)$, where $A_u(\mathbf{k}; E)$ is the spectral function of the upper layer. In a tunneling Hamiltonian approach, the two layers are assumed to be weakly coupled, so that each layer can be approximated as equilibrated with its own Fermi level. Then, $G_l^<(\mathbf{k}; E) = i f(E - \mu_l) A_l(\mathbf{k}; E)$, and Eq. (3.3) becomes

$$J = \frac{g_s g_v q}{hA} \sum_{\mathbf{k}} \int dE |t_{\perp}(\mathbf{k})|^2 A_u(\mathbf{k}; E) A_l(E; \mathbf{k}) \cdot [f(E - \mu_u) - f(E - \mu_l)]. \quad (3.4)$$

The spectral functions are given by $A_{u(l)} = \frac{\gamma}{(E - \varepsilon(\mathbf{k}))^2 + \frac{\gamma^2}{4}} = \frac{\gamma}{E_z^2 + \frac{\gamma^2}{4}}$ where γ is the lifetime broadening in each layer and in the second equality, we define $E_z \equiv E - \varepsilon(\mathbf{k})$. Since the interlayer coupling t_{\perp} is a weak function of \mathbf{k} , we use its value at the band edge. Then, we can perform the sum over the transverse momenta analytically, and Eq. (3.2) now has the form

$$J = \frac{g_s g_v q}{h} \frac{m^*}{2\pi\hbar^2} \int dE_z |t_{\perp}|^2 A_u(E_z) A_l(E_z) \cdot \int_0^{\infty} d\varepsilon [f(E_z + \varepsilon - E_{f,u}) - f(E_z + \varepsilon - E_{f,l})] \quad (3.5)$$

For small voltages, the difference in Fermi factors becomes $\frac{-\partial f}{\partial \varepsilon} qV$ where V is the applied voltage, and the integral over ε gives $f(E_z - E_f) qV$ where E_f is the equilibrium Fermi level.

Therefore, the 2D-2D tunneling formula for the interlayer conductivity is

$$\sigma_{2D} = \frac{g_s g_v q^2}{h} \frac{m^*}{2\pi\hbar^2} \int dE_z \frac{|t_\perp|^2 \gamma^2 f(E_z - E_f)}{\left[E_z^2 + \frac{\gamma^2}{4}\right]^2}. \quad (3.6)$$

All calculations of the electronic conductivity σ_{2D} use a value of $\gamma = 12.6$ meV, and it is estimated from the mobility lifetime using $\mu = e\tau/m^*$ and $\gamma = \hbar/\tau$. For the mobility, we chose 200 cm²/Vs, which is an average of the best measured value for a monolayer of 81 cm²/Vs [43] and the theoretical value of 320 cm²/Vs [44].

For a given transverse \mathbf{k} , the transmission resulting from this approach is $T(E; \mathbf{k}) = \frac{|t_\perp|^2 \gamma^2}{\left[(E - \varepsilon(\mathbf{k}))^2 + \frac{\gamma^2}{4}\right]^2}$ which has a maximum value of $16 |t_\perp|^2 / \gamma^2$. Since this value must be ≤ 1 , it sets an upper limit on the expression's validity in terms of the magnitude of the coupling with respect to the broadening, $|t_\perp| \leq \gamma/4 = 3.15$ meV. For the K_c valley, the unrotated structure does not satisfy this condition, since $t_\perp = 7.6$ meV; but for all non-zero rotation angles, this condition is satisfied. For the Γ_v valley at all rotation angles, it is not.

To have an expression that is also valid for the strongly coupled bands, we create a low-energy, 3D-3D transmission model for each band. Physically, this corresponds to a system of two semi-infinite stacks with one stack rotated with respect to the other resulting in the rotated interface depicted in Fig. 3.1(a). For each band, at each transverse \mathbf{k} , this model reduces to that of a one dimensional (1D) tight-binding chain as shown in Fig. 3.1(b). The hopping parameter t_0 is given by t_\perp of the unrotated bilayer in Fig. 3.2(a). For this model, the ‘device’ consists of the two misoriented layers numbered 0 and 1 in Fig. 3.1(b). The ‘device’ Hamiltonian for band ν is given by Eq. (3.1). The left and right self-energies

due to coupling to the semi-infinite leads are $\Sigma^R = t_0 e^{ik_z a}$. The Green function is

$$G^R = \begin{pmatrix} E - \varepsilon_\nu(\mathbf{k}) - t_0 e^{ik_z a} & -t_\perp^\nu(\mathbf{k}) \\ -t_\perp^\nu(\mathbf{k}) & E - \varepsilon_\nu(\mathbf{k}) - t_0 e^{ik_z a} \end{pmatrix}^{-1}. \quad (3.7)$$

The transmission is calculated from $T(E, \mathbf{k}) = \Gamma_u \Gamma_l |G_{0,1}^R(E, \mathbf{k})|^2$ where $\Gamma_l = \Gamma_u = 2|t_0| \sin(k_z a)$.

Using the dispersion relation of the leads, $E = \varepsilon_\nu(\mathbf{k}) + 2t_0 \cos(k_z a)$, this can be analytically

evaluated to obtain $T(E_z) = \frac{t_\perp^2 (4t_0^2 - E_z^2)}{(t_0^2 + t_\perp^2)^2 - t_\perp^2 E_z^2}$ where $E_z \equiv E - \varepsilon_\nu(\mathbf{k})$. Going through the same

steps as for the 2D-2D tunneling formula, the 3D-3D expression for the conductance is

$$\sigma_{3D} = \frac{g_s g_v q^2}{h} \frac{m^*}{2\pi \hbar^2} \int_{-2t_0}^{2t_0} dE_z \frac{t_\perp^2 (4t_0^2 - E_z^2) f(E_z - E_f)}{(t_0^2 + t_\perp^2)^2 - t_\perp^2 E_z^2}. \quad (3.8)$$

In all calculations of the interlayer conductance, the Fermi level is taken to be $k_B T$ below the conduction band edge when calculating the electron conductance or $k_B T$ above the valence band edge when calculating the hole conductance, with $T = 300\text{K}$. The interlayer resistivity ρ is the inverse of the conductivity calculated from Eqs. (3.6) or (3.8).

3.3 Results and Discussion

Fig. 3.3(b) shows the interlayer resistivity for electrons at the conduction band edge at K and the holes at the valence band edge at Γ . The interlayer resistivity for holes is only calculated from the expression for σ_{3D} in Eq. (3.8), since the 2D-2D tunneling formula is not valid for the holes due to the large value of $|t_\perp|$. The interlayer resistivity for electrons is calculated from both expressions, σ_{2D} from Eq. (3.6) and σ_{3D} , and the trends and quantitative values from both expressions match to within a factor of three over 3 orders of magnitude. The agreement is not too surprising since the conductivity

resulting from both expressions is proportional to t_{\perp}^2 , and the dependence of the electron and hole interlayer conductivity follows the dependence of the interlayer coupling shown in Fig. 3.3(a).

The physics of the interlayer coupling is determined by the periodic part of the Bloch function (the orbital composition), the phase or envelope $e^{i\mathbf{k}\cdot\mathbf{r}}$, and the interlayer trigonal arrangement of the 3 nearest neighbor Mo atoms in one layer with respect to a Mo atom in the other layer. We will first discuss the K valley and then the Γ valley.

First, consider the unrotated 2H bilayer. The very small interlayer coupling of the conduction band is due the symmetry of the conduction band Bloch functions at the K points. The conduction band edge at K is composed of predominantly Mo d_{z^2} orbitals. In a minimal basis, the Bloch state at the conduction band edge of an individual monolayer is $|K_c\rangle = \sum_{\mathbf{R}_n} |d_{z^2}; \mathbf{R}_n\rangle e^{i\mathbf{K}\cdot\mathbf{R}_n}$ where \mathbf{R}_n is the position of each Mo atom. The conduction band interlayer coupling is proportional to the the interlayer matrix element $\langle K_c, u | H | K_c, l \rangle = \langle d_{z^2}^u | H | d_{z^2}^l \rangle \sum_{n=1}^3 e^{i\mathbf{K}\cdot\mathbf{R}_n} \propto \sum_{n=0}^2 e^{in2\pi/3} = 0$ where $\langle d_{z^2}^u | H | d_{z^2}^l \rangle$ is the matrix element between interlayer, nearest neighbor, Mo d_{z^2} orbitals. Since the interlayer matrix element $\langle d_{z^2}^u | H | d_{z^2}^l \rangle$ is independent of the azimuthal angle, it is pulled outside of the sum, and the sum of the three phase factors exactly cancel. (For an expanded discussion, see the Supplementary Information of [12].)

In contrast, the valence band state at K is composed of d_{xy} and $d_{x^2-y^2}$ orbitals. The interlayer matrix elements between these orbitals change sign as a function of the azimuthal angle preventing the cancellation of the phase factors. Therefore, at the K valley of the unrotated structure, even though the conduction band orbitals are out-of-plane and

the valence band orbitals are in-plane, the interlayer coupling at K_c is an order of magnitude smaller than the interlayer coupling at K_v , as shown in Fig. 3.3(a).

Two mechanisms compete to determine the effect of interlayer rotation on the conduction band coupling at K . When one layer is rotated with respect to the other, the symmetry is broken, and the exact cancellation of the phases is destroyed. This effect would cause the matrix element to increase. However, now the unit cell size has increased to one of the supercells shown in Fig. 3.1, and the interlayer matrix elements between all of the d_{z^2} orbitals in the supercell and their associated phase factors must be added. At K , the phase is changing sign approximately every lattice constant, so that as the wavefunction of the top layer is rotated with respect to that of the bottom layer, and the phases are summed over the large supercell, the matrix element is suppressed by phase cancellation. These two competing effects cause the initial slower decrease in the coupling of the conduction band at K compared to the coupling of the valence band at K as shown in Fig. 3.3(a).

The effect of misorientation on the the interlayer resistivity of the electrons at K is similar to the effect of misorientation on the interlayer resistivity of electrons and holes in bilayer graphene [45, 38, 46]. The electron resistivity increases exponentially with the size of the supercell lattice constant, although the increase in MoS₂ is orders of magnitude less than the increase in bilayer graphene (compare Fig. 1d of [38] or Fig. 4 of [46] with Fig. 3.3(b)).

The valence band edge at Γ is composed of 28% S p_z orbitals and 67% Mo d_{z^2} orbitals[13]. These out-of-plane orbitals, especially the p_z orbitals on the surface S atoms, strongly couple between layers. Furthermore, the interlayer matrix elements are indepen-

dent of the azimuthal angle, and at Γ , all of the phase factors are 1, so the matrix elements add, and the interlayer coupling is large as shown in Fig. 3.3(a).

When one layer is rotated with respect to the other, no phase cancellation can occur, since the Γ wavefunctions have no phase. Thus, the holes at Γ are minimally affected by layer rotation. The only effect on the hole coupling is through the slight increase in the interlayer separation causing a slight decrease in the interlayer coupling as shown in Fig. 3.3(a). Furthermore, the interlayer coupling of the holes monotonically decreases with angle rather than with supercell size, following the monotonic increase of the interlayer distance (see Table S1), which further indicates that different physics govern the effect of misorientation on the electron and hole interlayer coupling.

To gain perspective into what the resistivity values mean for a device application, we consider the target resistivity value of $2.5 \Omega\mu\text{m}^2$ for the emitter contact resistance required to achieve THz cutoff frequency in a heterostructure bipolar transistor (HBT) [47]. The interlayer resistivity of the holes is approximately equal to or below that value for all angles. For all non-zero rotation angles considered, the interlayer resistivity of the electrons is one or more orders of magnitude too high. This suggests design optimization of a heterostructure bipolar transistor (HBT) using stacked TMDs. A pnp HBT will be insensitive to misalignment of the layers. Furthermore, rotating the emitter layer with respect to the base layer in a pnp HBT will increase the emitter injection efficiency by one or more orders of magnitude, since the transmission of electrons injected from the base will be suppressed while the transmission of holes injected from the emitter will be unaffected.

With negligible recombination in the base, the ratio of the hole current to electron

current, I_E/I_B , is the low-frequency gain β of the HBT, so that an increase in I_E/I_B is an equivalent increase in β . In a circuit model, the interlayer resistance is in series with the base-emitter diode, so that if the resistance of the base-emitter diode is much greater than the interlayer resistance, the effect of changing the interlayer resistance is negligible.

To compare quantitative values, we consider the ac resistance of the junction for the holes (r_p) and electrons (r_n) defined by $r_p = (\partial I_E / \partial V_{EB})^{-1}$ and $r_n = (\partial I_B / \partial V_{EB})^{-1}$, respectively. In the on-state, $I_E = I_{0,E} e^{V_{EB}/V_T}$ and $I_B = I_{0,B} e^{V_{EB}/V_T}$ where $V_T = k_B T / q$, so that the ac resistances due to the pn junction are $r_p = V_T / I_E$ and $r_n = V_T / I_B$. Now, consider a homo junction BJT with an equally doped base and emitter, so that $r_n \approx r_p$. Such a device would traditionally have a gain < 1 . Target high-frequency emitter current densities [47] range from approximately 4.5 mA/ μm^2 to 36 mA/ μm^2 giving corresponding values for r_p of 5.8 $\Omega\mu\text{m}^2$ and 0.72 $\Omega\mu\text{m}^2$, respectively. The total resistance (junction plus interface) seen by the holes is $r_p + R_{\text{int}}^p$ and the total resistance seen by the electrons is $r_n + R_{\text{int}}^n$. The ac hole current is $i_E = v_{EB} / (r_p + R_{\text{int}}^p)$, the ac electron current is $i_B = v_{EB} / (r_n + R_{\text{int}}^n)$, and the ac gain is $i_E / i_B = (r_n + R_{\text{int}}^n) / (r_p + R_{\text{int}}^p)$. Choosing values from $\theta = 27.79^\circ$ in Fig. 3.3(b), $R_{\text{int}}^p = 2.7 \Omega\mu\text{m}^2$, and $R_{\text{int}}^n = 250 \Omega\mu\text{m}^2$. If we take the least aggressive value of $r_p = 5.8 \Omega\mu\text{m}^2$, then $i_E / i_B = 30$. Thus, for high current density devices, the asymmetrical electron and hole interface resistances due to interface rotation give an ac gain of 30 for equal emitter and base doping in the absence of a heterojunction, and the value increases as the current density increases. Such a result has previously only been possible through the use of an emitter-base heterojunction consisting of a wider bandgap emitter and a narrower bandgap base.

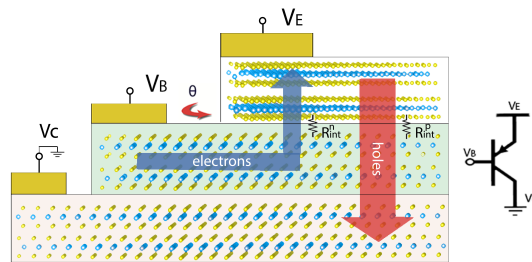


Figure 3.4: A vertical pnp BJT with the emitter rotated with respect to the base. The flow of electrons and holes are shown along with their interface resistances, R_{int}^n and R_{int}^p . The pnp circuit symbol is shown at right.

Chapter 4

Modeling of Tunable Lifshitz Transitions and Multiband Transport in Tetralayer Graphene

4.1 Introduction

In this work, we focus on numerical analysis of a relatively unexplored 2D multi-Dirac band system, Bernal-stacked tetralayer graphene(4LG). Its band structure can be decomposed into intersecting bilayer graphene (BLG)-like bands with light and heavy effective masses, which are hybridized at low energies due to next-nearest-layer hopping. The hopping term γ_3 between skewed lattice sites in adjacent layers gives rise to trigonal warping that persists to relatively large energies. The co-presence of both bands, combined with trigonal warping, provides a tunable platform in which the Lifshitz transitions(LT)

is readily accessible. Using tight binding calculations, multiband transport calculation, we provide numerical analysis on dramatic features in transport characteristics, including non-monotonic dependence of conductivity on charge density n and out-of-plane electric field D , anomalous quantum Hall (QH) sequences and Landau level(LL) crossings. These features are identified to arise from as many as six different changes in topology of Fermi contours and multiband transport as n, D , and B are varied.

In this dissertation, we focus on the modeling and analysis of the results. Collaborative experimental results are published at PRL [2].

4.2 Transport properties

Figure 4.1(a) displays the longitudinal resistance R of 4LG as a function of n and D in the absence of a magnetic field. At the charge neutrality point (CNP), R first increases symmetrically with D , indicating the opening of a band gap due to the broken inversion symmetry, then saturates at larger $D > \sim \pm 220 \text{ mV/nm}$ [Fig. 4.1(b)]. This is consistent with the theoretically predicted opening of a small band gap that saturates at $\sim 5 \text{ meV}$ for large D [48].

A close examination of Fig. 4.1(a) reveals several rather surprising features. In particular, what immediately sets it apart from thinner graphene devices is that, instead of a single peak at the CNP, $R(n)$ of 4LG exhibits three peaks, which are labeled as X , Y , and Z , respectively [Fig. 4.1(c)]. The leftmost peak X is the most prominent, and rightmost peak Z is present as a small shoulder. Such nonmonotonic $R(n)$ behavior points to the underlying multibands of tetralayer graphene that are more complex than its thinner

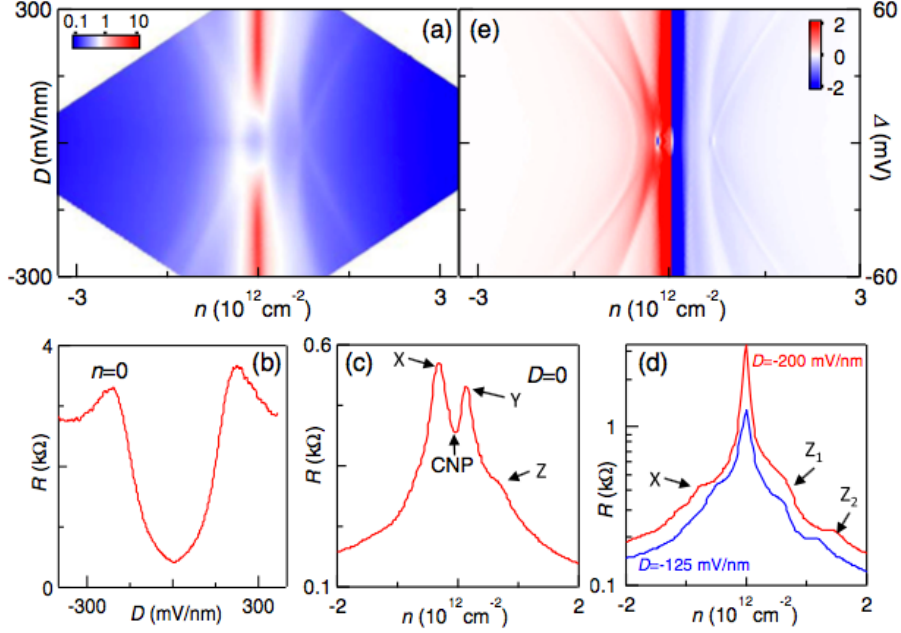


Figure 4.1: (a) Longitudinal resistance map $R(n, D)$ in log scale at $B = 0$. The unit is $k\Omega$. (b) Line trace $R(D)$ at the CNP. (c)(d) Line traces $R(n)$ at $D = 0$ (c), -200 [(d), red] and -125 (d, blue) mV/nm , respectively. The traces are offset by $0.2k\Omega$ for clarity in (d). The black arrows indicate the peaks and the CNP. (e) Differentiated simulated $dR/dn(n, D)$ using Boltzman transport theory at the same charge density as (a).

graphene counterparts [4, 6, 49, 50, 51, 52, 53]. In fact, the charge neutrality point (CNP), as determined from the peak in R at large D , is not located at any of the three peaks at $D = 0$. Instead, it corresponds to a local resistance minimum located between peaks X and Y [Fig. 4.1(c)]. This identification of the CNP with a local resistance minimum represents yet another ‘deviation’ from the standard behaviors of monolayer, bilayer, and trilayer graphene devices, where the CNP is invariably associated with a resistance peak [4, 6, 49, 51, 53, 54]. Another unexpected feature is the intricate dependence of the peaks on D : as $|D|$ increases, peak X appears to move to larger charge density, while peak Z splits into two peaks Z_1 that is relatively stationary in D , and Z_2 that moves linearly with D . The movement of the peaks X and Z_2 can be clearly seen in line traces $R(n)$ at $D = -125$

and $-200mV/nm$ [Fig. 4.1(d)].

For modeling of the transport properties, we use Boltzmann transport theory. In Boltzmann transport theory, the conductivity can be written as a sum of intraband and interband contributions[26]:

$$\sigma_{intra}^{xx} = e^2\tau \sum_n \int_{BZ} \frac{1}{(2\pi)^2} d\theta k dk |\langle n\mathbf{k} | \frac{\partial \mathbf{H}}{\partial \mathbf{k}_x} | n\mathbf{k} \rangle|^2 \left(-\frac{\partial f_{n\mathbf{k}}}{\partial \epsilon_{n\mathbf{k}}} \right) \quad (4.1)$$

$$\sigma_{inter}^{xx} = ie^2\hbar \sum_{n,m \neq n} \int_{BZ} \frac{1}{(2\pi)^2} d\theta k dk \frac{f_{m\mathbf{k}} - f_{n\mathbf{k}}}{\epsilon_{n\mathbf{k}} - \epsilon_{m\mathbf{k}}} \frac{\langle n\mathbf{k} | \frac{\partial \mathbf{H}}{\partial \mathbf{k}_x} | m\mathbf{k} \rangle \langle m\mathbf{k} | \frac{\partial \mathbf{H}}{\partial \mathbf{k}_x} | n\mathbf{k} \rangle}{\epsilon_{n\mathbf{k}} - \epsilon_{m\mathbf{k}} + i\hbar\tau^{-1}} \quad (4.2)$$

where the $\epsilon_{n\mathbf{k}}$ and $f_{n\mathbf{k}}$ are the energy and Fermi-Dirac distribution function of band n with wave vector k . We treat the relaxation time τ as an independent parameter and assume that τ is the same for both intraband and interband scattering mechanisms[26].

4.3 Band structures with topology analysis

For the analysis of ABAB stacked tetralayer graphene from band structure perspective, a tight binding model calculation is carried out. The Hamiltonian in the vicinity of the K_ξ valley is:

$$H = \begin{bmatrix} \frac{eD \cdot d}{2} & v\pi^\dagger & -v_4\pi^\dagger & v_3\pi & \frac{\gamma_2}{2} & 0 & 0 & 0 \\ v\pi & \delta + \frac{eD \cdot d}{2} & \gamma_1 & -v_4\pi^\dagger & 0 & \frac{\gamma_5}{2} & 0 & 0 \\ -v_4\pi & \gamma_1 & \delta + \frac{eD \cdot d}{6} & v\pi^\dagger & -v_4\pi & \gamma_1 & \frac{\gamma_5}{2} & 0 \\ v_3\pi^\dagger & -v_4\pi & v\pi & \frac{eD \cdot d}{6} & v_3\pi^\dagger & -v_4\pi & 0 & \frac{\gamma_2}{2} \\ \frac{\gamma_2}{2} & 0 & -v_4\pi^\dagger & v_3\pi & -\frac{eD \cdot d}{6} & v\pi^\dagger & -v_4\pi^\dagger & v_3\pi \\ 0 & \frac{\gamma_5}{2} & \gamma_1 & -v_4\pi^\dagger & v\pi & \delta - \frac{eD \cdot d}{6} & \gamma_1 & -v_4\pi^\dagger \\ 0 & 0 & \frac{\gamma_5}{2} & 0 & -v_4\pi & \gamma_1 & \delta - \frac{eD \cdot d}{2} & v\pi^\dagger \\ 0 & 0 & 0 & \frac{\gamma_2}{2} & v_3\pi^\dagger & -v_4\pi & v\pi & -\frac{eD \cdot d}{2} \end{bmatrix} \quad (4.3)$$

where the D is the vertical electric field, d is the thickness of tetralayer graphene, ξ is the valley index, and $\pi = \xi p_x + i p_y$ is the momentum operator. The Fermi velocity of graphene is $v = \frac{\sqrt{3}a\gamma_0}{2\hbar}$, and the related velocities are $v_3 = \frac{\gamma_3}{\gamma_0}v$, $v_4 = \frac{\gamma_4}{\gamma_0}v$.

The hopping parameters are extracted by matching the LL crossing points between experimental data $R(n, B)$ over a wide range of B at $D = 0$ and LL spectra that are calculated using a $k \cdot p$ continuum model. Figure 4.2(b) displays the three-dimensional (3D) band structure and its 2D projection at $D = 0$, respectively. At higher energies, the bands are well approximated by two intersecting BLG-like bands with different effective masses. The band structure calculated by ignoring the off-diagonal blocks in the Hamiltonian is plotted as the dotted lines in Fig. 4.2(b), showing the outlines of the intersecting bands.

At low energies, the next-nearest-neighbor hoppings hybridize the bands [solid lines, Fig. 4.2(b)]. In particular, as a result of the skewed hopping term γ_3 , trigonal warping significantly distorts the band structure [55, 56, 57, 58] as we tune the Fermi level

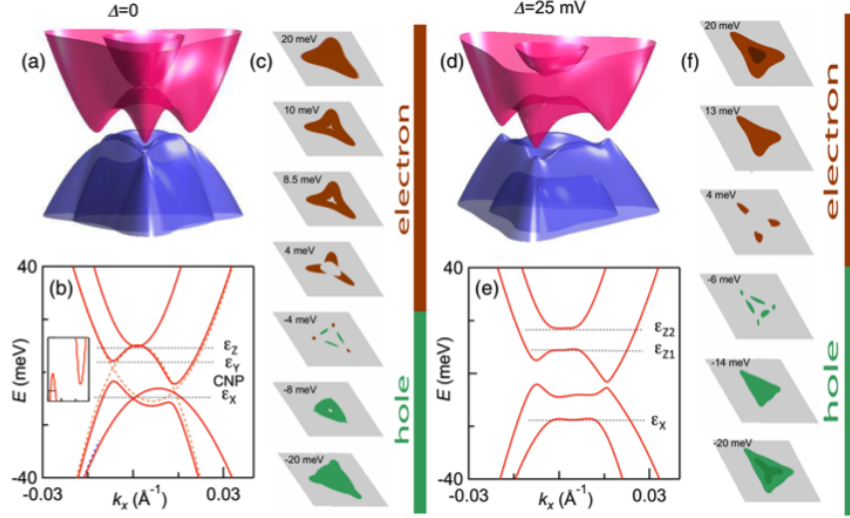


Figure 4.2: (a)(b) Calculated 3D band structure and its 2D projection $E(k_x)$ at $\Delta = 0$, respectively. In (b), the inset displays the overlap of conduction and valance bands at the CNP. Horizontal dashed lines indicate the energy levels corresponding to the Lifshitz transition points. The red solid and dotted lines are calculated by taking the full Hamiltonian and neglecting the off-diagonal block in the Hamiltonian, respectively. (c) A series of cross sections of band structure showing evolution of the Fermi surfaces by tuning Fermi energy at $\Delta = 0$. (d)(e) Calculated 3D band structure and 2D projection $E(k_x)$ at $\Delta = 25mV$. A band gap at the CNP is opened, and the accidental degeneracy at the intersecting point between two BLG-like bands is broken. The dashed black lines in (e) indicate the energy levels corresponding to the Lifshitz transition points. (f) Evolution of Fermi surfaces at $\Delta = 25mV$ as a function of Fermi energy.

E_F of 4LG by gating, the topology of the Fermi surfaces changes, leading to anomalies in the resistance. A series of cross sections of the band structure showing the Fermi surface evolution is plotted in Fig. 4.2(c). For instance, at the CNP, 4LG is a semimetal with overlapping conduction and valance bands [Fig. 4.2(b), inset]; its Fermi surface consists of three elongated pockets of holes and three circular pockets of electrons, which occupy the edges and vertices of a triangle, respectively. These pockets of electrons and holes are isolated from one other. As more holes enter the device, the electron pockets disappear while the three disjoint hole pockets expand. When E_F is lowered past the point at which

the light mass and heavy mass bands intersect, $E = -10meV$, the Fermi surface morphs from a doubly connected triangle with a hole in the center to a singly connected triangle. This abrupt change in the topology of the Fermi surface is reflected in the $R(n, B)$ data, and is associated with the resistance peak X in Fig. 4.1. Similarly, when E_F increases from the CNP to $\sim 4.6meV$, the resistance peak Y accompanies the LT as the topology of the Fermi surface evolves from three disjoint pockets of electrons to a doubly connected triangle; with a further increase of E_F to $10meV$, the Fermi surface evolves into a singly connected triangle with the presence of both BLG-like bands, giving rise to the resistance peak Z . These energies are labeled ϵ_X , ϵ_Y , and ϵ_Z in Fig. 4.2(b), respectively. In other words, each of the three peaks in resistance, as well as the minimum at the CNP, are associated with distinct LTs as the Fermi energy varies.

Upon the application of an interlayer potential difference Δ , 4LG's inversion symmetry is broken, leading to nontrivial modification of the band structure. For instance, for $\Delta > 20$ mV, a small band gap opens, giving rise to the observed high resistance at the CNP. Figures 4.2(d)-4.2(e) plot the 3D band structure and 2D $E(k_x)$ at $\Delta = 25mV$, respectively, while Fig. 4.2(f) plots the evolution of Fermi surfaces at $\Delta = 25mV$. Note that Δ denotes the actual potential bias across the 4LG; because of screening, it is typically much smaller than that imposed by external gates Dd , where $d \sim 1nm$ is the separation between the outmost layers. The Lifshitz transition persists at finite Δ -when E_F moves away from conduction and valence band edges the topology of the Fermi surface changes from three disjoint pockets to a hollow triangle, to finally a singly connected triangle.

Another important effect of Δ is the lifting of the accidental degeneracies at ϵ_Z

and ϵ_X , as it causes the light-mass bands to split away from zero energy. In other words, the two intersecting BLG-like bands at $\Delta = 0$ split into two subbands, with energetic separations that approximately scale with Δ . Alignment of the Fermi level with the edges of the second subbands, which host electrons with very low velocities, provide additional channels for scattering, thus leading to the resistance peaks at the corresponding charge densities; i.e., this degeneracy breaking by $\Delta = 0$ gives rise to the split peaks Z_1 and Z_2 in the electron-doped regime, and X in the hole-doped regime. Quantitatively, we use the Boltzmann transport theory to calculate 4LG's resistivity as a function of n and interlayer potential Δ , as shown in Fig. 4.1(e). The simulation satisfactorily reproduces the major features in the data. To account for the local minimum resistance at the CNP, we take the interband scattering between conduction and valance bands into account, which produces a local resistivity minimum near $n = D = 0$, suggesting that such interband scattering may play an important role in the transport of 4LG, particularly at the CNP.

Chapter 5

Edge States in Trilayer Graphene Nanoribbons

5.1 Introduction

Since the exfoliation of first monolayer graphene, graphene has attracted great interest in its electronic properties and in its ability to serve as a platform for rich physics [4, 5, 6]. The quantum hall states including integer quantum hall state, fractional quantum hall state, and the quantum spin hall state have all been well studied both experimentally and theoretically in monolayer graphene or bilayer graphene [5, 50, 51, 52, 53, 54, 55]. Recently, there has been interest in the quantum mirror hall state in trilayer graphene because of its unique structure symmetry [53, 59]. The interplay between the electric field and the magnetic field in a trilayer graphene nanoribbon modifies the bulk and edge states of the system. As seen in experiments [60], the change in band structures will result in four

different quantum phases (including a quantum parity Hall state, a quantum mirror Hall ferromagnetic metal, a quantum valley Hall (QVH) insulator, and layer polarized insulator states) with different conducting behavior. For the novel quantum parity Hall (QPH) effect, boundary channels are distinguished by even or odd parity under the system's mirror reflection symmetry, which can be found in ABA-stacked trilayer graphene at the charge neutrality point.

For the measurement of two-probe longitudinal conductances σ_{xx} in experiments with approximate ballistic conductance as shown, quantized conductance is first realized at low B_{\perp} where $\sigma_{xx} = 4e^2/h$ establishing the presence of four edge channels traveling from source to drain. As B_{\perp} increases the quantized conductance decreases first to $\sigma_{xx} = 2e^2/h$ and then to small values.

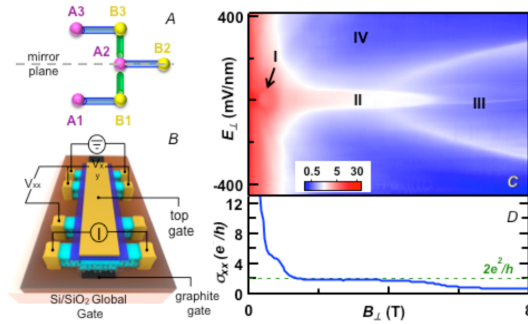


Figure 5.1: (a) Schematics of hBN-encapsulated TLG device. (b) Phase diagram $\sigma_{xx}(E_{\perp}, B_{\perp})$ at the CNP and $T = 260mK$. The different electronic phases are labeled *I* through *IV*.

In trilayer graphene, the electronic bands can be decoupled into a combination of bilayer-like bands and dirac-like bands, and with mirror symmetry, the system exhibits quantized longitudinal conductance at the charge neutrality point, due to counterpropagating even and odd parity edge modes [3, 59]. Here we used a tight binding model to

investigate more of the properties of edge states in trilayer graphene nanoribbons and provide insight into quantum mirror hall states and their dependence on electric field and magnetic field as observed in experimental results from collaborating groups.

5.2 Tight banding calculations

In the absence of external bias, the band structure of the trilayer graphene consists of monolayer-like and bilayer-like bands in a new basis of $\{\frac{A_1-A_3}{\sqrt{2}}, \frac{B_1-B_3}{\sqrt{2}}, \frac{A_1+A_3}{\sqrt{2}}, B_2, A_2, \frac{B_1+B_3}{\sqrt{2}}\}$ [25]. In the new basis, the sum of two terms, $H_0 + H_{\Delta_2}$ acquires a block-diagonal structure:

$$H_0 + H_{\Delta_2} = \begin{bmatrix} H_{SLG} & 0 \\ 0 & H_{BLG} \end{bmatrix} \quad (5.1)$$

where the monolayer-like and bilayer-like blocks are defined as

$$H_{SLG} = \begin{bmatrix} \Delta_2 - \frac{\gamma_2}{2} & v_0\pi^\dagger \\ v_0\pi & -\frac{\gamma_5}{2} + \delta + \Delta_2 \end{bmatrix} \quad (5.2)$$

$$H_{BLG} = \begin{bmatrix} \Delta_2 + \frac{\gamma_2}{2} & \sqrt{2}v_3\pi & -\sqrt{2}v_4\pi^\dagger & v_0\pi^\dagger \\ \sqrt{2}v_3\pi^\dagger & -2\Delta_2 & v_0\pi & -\sqrt{2}v_4\pi \\ -\sqrt{2}v_4\pi & v_0\pi^\dagger & \delta - 2\Delta_2 & \sqrt{2}\gamma_1 \\ v_0\pi & -\sqrt{2}v_4\pi^\dagger & \sqrt{2}\gamma_1 & \Delta_2 + \frac{\gamma_5}{2} + \delta \end{bmatrix} \quad (5.3)$$

The effective Hamiltonian of the bilayer-like part can be simplified further by noting that the low-energy states predominantly reside on $A_1 + A_3$ and on B_2 sublattices. Then the effective 2×2 Hamiltonian of the bilayer-like band:

$$H_{BLG} \approx H_{BLG}^{(0)} + H_{BLG}^{(1)} \quad (5.4)$$

$$H_{BLG}^{(0)} = -\frac{1}{2m} \begin{pmatrix} 0 & \pi^{\dagger 2} \\ \pi^2 & 0 \end{pmatrix} \quad (5.5)$$

$$H_{BLG}^{(1)} = \sqrt{2}v_3 \begin{pmatrix} 0 & \pi \\ \pi^{\dagger} & 0 \end{pmatrix} + \begin{pmatrix} \frac{\gamma_2}{2} + \Delta_2 & 0 \\ 0 & -2\Delta_2 \end{pmatrix} + \frac{v^2}{2\gamma_1} \begin{pmatrix} (\delta - 2\Delta_2)\pi^{\dagger}\pi & 0 \\ 0 & (\frac{\gamma_5}{2} + \delta + 2\Delta_2)\pi\pi^{\dagger} \end{pmatrix} \quad (5.6)$$

In our practical simulations, as presented in chapter 2, with Slonszewski-Weiss-McClure parameters, a rectangular unit cell with atoms

$$\{A_1, B_1, A_2, B_2, A_3, B_3, A'_1, B'_1, A'_2, B'_2, A'_3, B'_3\} \quad (5.7)$$

is chosen for modeling instead of regular unit cell. Moreover, to calculate the bands, the total Hamiltonian matrix is divided into small parts as $\alpha_u, \beta_0, \beta_1, \beta_2$ and t . They are Hamiltonians of unit cell blocks and interactions between blocks. For different nanoribbon edges, different α (Hamiltonian of supercell) and β (interactions between supercells) are constructed accordingly. In order to decouple even and odd bands when no electric field is applied, a transformation matrix M is used to change the basis. Finally, the Hamiltonian is $H(k) = \alpha + \beta' e^{-ka} + \beta e^{ka}$.

With applied perpendicular B-field $(0, 0, B_z)$, a vector potential $(-B_z y, 0, 0)$ or $(0, -B_z x, 0)$ is used accordingly based on the edge. The Peierls phase factor and the interactions will be calculated accordingly. The electrical potential $\Delta_{E_{\perp}}$ will change the diagonal elements of the Hamiltonian.

5.3 Results and Discussion

For trilayer graphene, the electronic bands could be decoupled into a combination of bilayer-like bands and dirac-like bands as below. The relative positions of bands are well examined and used for parameter tuning.

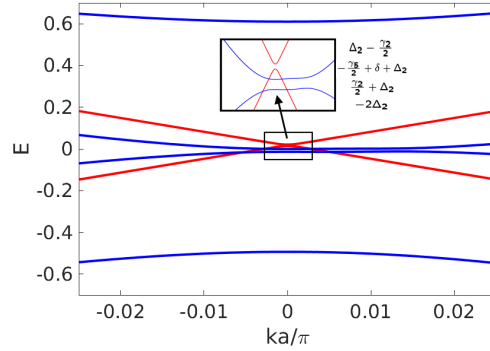


Figure 5.2: Bands of trilayer graphene decoupled into monolayer-like(red) and bilayer-like(blue) bands.

Edge states in zigzag and armchair edge nanoribbons share similar properties within magnetic field. Thus, we take the calculation results of zigzag edge trilayer graphene nanoribbon with width of about $200nm$ as an example. From Fig. 5.3(a), under magnetic field $B_{\perp} = 8T$ and $E_{\perp} = 0$, the bands of the nanoribbon are decoupled into odd and even parity bands. At low energy, the wave functions for the decoupled bands in the solid box in Fig. 5.3(a) are $\{\frac{B_1-B_3}{\sqrt{2}}, \frac{A_1-A_3}{\sqrt{2}}, B_2, \frac{A_1+A_3}{\sqrt{2}}\}$, and they are counter propagating in separate channels. With a external electric field E_{\perp} of $30meV$ between layers, the wave functions become hybridized and the energies are slightly shifted. **Here, ΔE_{\perp} is the potential difference induced by vertical electric field and is simplified as E_{\perp} .** Since the mirror symmetry is now broken, Fig. 5.3(b) shows small gaps appearing at the

band crossings. The change of the bands are small, while the gap and state hybridization changes abruptly with symmetry. With a finite displacement field, backscattering between counter propagating states becomes allowed, and thus the conductance quickly reduces to a small value as observed in experimental data.

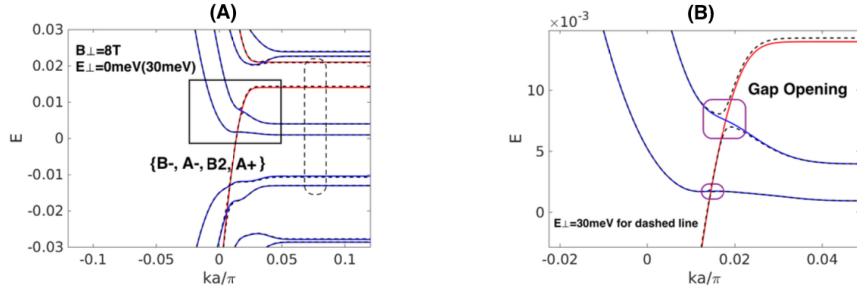


Figure 5.3: Bands of zigzag edge trilayer graphene nanoribbon with and without external electric field E_{\perp} .

Our simulation results also provide insight into the trends of the change of the relative positions of the bands and their dependence on different external electric and magnetic field. For an electric field, the Hamiltonian introduced by E_{\perp} is $\Delta H = (E_{\perp}|A_1\rangle\langle A_1| + E_{\perp}|B_1\rangle\langle B_1|) - (E_{\perp}|A_3\rangle\langle A_3| + E_{\perp}|B_3\rangle\langle B_3|)$. For low energy bands, $|\frac{A_1-A_3}{\sqrt{2}}\rangle$ and $|\frac{B_1-B_3}{\sqrt{2}}\rangle$ are odd parity states, and $|\frac{A_1+A_3}{\sqrt{2}}\rangle$ and B_2 are even parity states. Thus ΔH will have little effect on even parity bands and more effect on odd parity bands, which is consistent with our simulation results as in Fig. 5.4(A) where the odd parity bands change linearly as a function of E_{\perp} .

With external magnetic field B_{\perp} , the Landau levels of even parity bands become degenerate because of higher Landau levels hybridization. For the bands with higher order Landau level components, the dependence of the band energies is almost linear as seen in

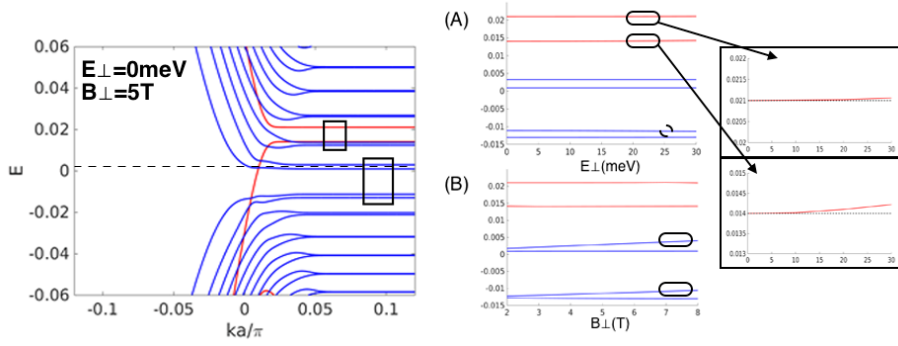


Figure 5.4: Changes of bands of zigzag edge trilayer graphene nanoribbon in dependence of electric field E_{\perp} and magnetic field B_{\perp} .

bilayer graphene, which is also consistent with literature and theory [61].

The simulations also demonstrate the mechanisms behind the phase transitions, which includes exchange interactions with the underlying Fermi sea that favor an ordinary insulator ground state at strong B_{\perp} and a spin-polarized intermediate state and varying Zeeman energy. Successively, for phase I (quantum parity Hall), the approximately spin-degenerate counter-propagating edge states are protected against backscattering by an underlying crystalline symmetry, since they correspond to different representations of the mirror reflection symmetry of the TLG crystal lattice that is preserved at $E_{\perp} = 0$. For phase II (quantum mirror Hall ferromagnetic metal), it has counterpropagating edge states with opposite spin and opposite parity caused by a change of bands, which are modified by an external magnetic field and Coulomb interactions. For even larger B_{\perp} , when both spin polarizations of the former are occupied and both spin polarizations of the latter are empty, there are no longer counter-propagating edge states, as all the even-parity electron LLs are above the odd-parity hole LLs, there will be a phase transition from phase II to phase III (QVH insulator). Thus, these phases arise from an intricate interplay between spin and

crystalline symmetries, localization, Zeeman energy, exchange interactions and self-energies of bands with different parities.

Chapter 6

Conclusions

The critical findings are summarized as follows:

- In misoriented MoS₂, the interlayer electron resistivity changes by 4 to 5 orders of magnitude as a function of the interlayer twist angle, and it scales exponentially with the size of the commensurate unit cell. The physics is the same as that governing the interlayer transport in rotated bilayer graphene. The wave functions at K have a rapidly varying phase. When the layers are rotated, there is strong quantum interference between the wave functions in the two layers resulting in destructive interference and exponentially reduced transmission and conductance. The hole resistivity at Γ is unaffected by rotation. The holes at Γ have no phase, so there is no quantum interference, and the interlayer hole transport is unaffected by rotation between the layers;
- Bernal-stacked 4LG is a highly tunable system with a single element, which constitutes an ideal platform for exploring the Lifshitz transition that is manifest as a

nonmonotonic dependence of conductivity on the charge density n and out-of-plane electric field D , anomalous quantum Hall sequences and Landau level crossings that evolve with n , D , and B ;

- With tight binding modeling, we provide analysis to explain the rich phase diagram including Quantum Parity(Mirror) Hall at the charge neutrality point in ABA-stacked TLG; and the intricate interplay between spin and crystalline symmetries, localization, Zeeman energy, exchange interactions and self-energies of bands with different parities for more insight on further experimental work.

Appendices

A DFT calculation for misoriented MoS₂

Electronic structure calculations of bilayer MoS₂ are carried out using density functional theory (DFT) with a projector augmented wave method and the Perdew-Burke-Ernzerhof (PBE) type generalized gradient approximation as implemented in the Vienna Ab initio Simulation Package (VASP) [62, 63, 64, 65, 66]. A semi-empirical Grimme-D2 correction to the Kohn-Sham energies is used to model the van der Waals (vdW) interactions [67]. Spin-orbit coupling is not included, since it has little effect on the interlayer coupling parameter, which is determined by orbital overlap. The plane wave basis energy cutoff is 400 eV. The global break condition for the electronic SC-loop is below 10^{-6} eV. The Monkhorst-Pack scheme is used for the integration over the Brillouin zone with a Γ centered k-mesh of $12 \times 12 \times 1$ for the unrotated thin films. For rotated bilayers, k-mesh are accordingly revised to $3 \times 3 \times 1$ for 13.17° , $6 \times 6 \times 1$ for 21.78° , $4 \times 4 \times 1$ for 27.79° , since they have different Brillouin zones. The k-space integration was carried out with a Gaussian smearing width of 0.02 eV for all calculations. All unit cells were built with 20 Å separation between replicas in the perpendicular direction to achieve negligible interaction. The default optimization methods did not efficiently determine the bilayer separation because the van der Waals interaction energies are very small. In order to accurately determine the bilayer separation of each system, several specific layer separations were used to optimize the structures until all or the interatomic forces are below $0.01 \text{ eV}/\text{Å}$ as described in the Supplementary Information of [29]. The optimized structure with lower total energy was chosen for structure of each

Angle θ	a/a_0	d (Å)	$E_{\Gamma-K}$ (eV)	E_{K-K} (eV)
2H(0)	1.0	6.2568	1.3650	1.7348
13.17°	$\sqrt{19}$	6.5142	1.5279	1.7683
21.78°	$\sqrt{7}$	6.5287	1.5339	1.7669
27.79°	$\sqrt{13}$	6.5853	1.5617	1.7698

Table S1: Interlayer distance (d), supercell lattice constant a , indirect energy gap $E_{\Gamma-K}$, and direct gap E_{K-K} as a function of rotation angle.

rotated angle. The interlayer distances of the relaxed structures are shown in Table S1.

B Codes and scripts for modeling

The codes and scripts used for all the projects can be found in my github [68].

Here are main MATLAB codes for modeling of edge states in trilayer graphene nanoribbon for future reference:

For Peierls phase factor:

```
1 % If added constant Bz magnetic field, change hamiltonian components:
2 Bz = input('Magnetic field Bz: ');
3 Basis = input('Basis used(1 for odd&even;2 for mixed): ');
4
5 % ignore z positions for calculation
6 A1 = [0,0];
7 B1 = [-1/2,sqrt(3)/2]*a;
8 A1_p = [3/2,sqrt(3)/2]*a;
9 B1_p = [1,0]*a;
10 A2 = [-1/2,sqrt(3)/2]*a;
11 B2 = [-1,0]*a;
12 A2_p = [1,0]*a;
13 B2_p = [1/2,sqrt(3)/2]*a;
14 A3 = [0,0];
15 B3 = [-1/2,sqrt(3)/2]*a;
16 A3_p = [3/2,sqrt(3)/2]*a;
17 B3_p = [1,0]*a;
18
19 Xlist = a*[0,-1/2,3/2,1,-1/2,-1,1,1/2,0,-1/2,3/2,1];
```

```

20 Ylist = a*[0,sqrt(3)/2,sqrt(3)/2,0,sqrt(3)/2,0,\\
21 0,sqrt(3)/2,0,sqrt(3)/2,sqrt(3)/2,0];
22 Alpha_1 = kron(diag(ones(1,NW)),alpha)+kron(diag(ones(1,NW- ...
        1),1),beta0')+kron(diag(ones(1,NW-1),-1),beta0);
23 Beta_plus_1 = kron(diag(ones(1,NW)),t')+kron(diag(ones(1,NW- ...
        1),1),beta2')+kron(diag(ones(1,NW-1),-1),beta1);
24 Alpha_2 = kron(diag(ones(1,NW)),alpha)+kron(diag(ones(1,NW- ...
        1),1),t)+kron(diag(ones(1,NW-1),-1),t');
25 Beta_plus_2 = kron(diag(ones(1,NW)),beta0')+kron(diag(ones(1,NW- ...
        1),1),beta1')+kron(diag(ones(1,NW-1),-1),beta2');
26
27 %Armchair Structure for GNR
28 if ((type == 1)&&(device == 1))
29     Alpha = Alpha_1;
30     Beta = Beta_plus_1;
31 elseif ((type == 2)&&(device == 1))
32
33 %Zigzag Structure for GNR
34     Alpha = Alpha_2;
35     Beta = Beta_plus_2;
36 elseif ((type == 1)&&(device == 2))
37 end
38
39 l1 = sqrt(3)*a;
40 l2 = 3*a;
41
42 if (type == 1)

```

```

43
44 fprintf('using gauge1 \n');
45 % Modify alpha
46 for i = 1:NU*NW
47     for j = 1:NU*NW
48         ii = floor((i-0.5)/NU);
49         jj = floor((j-0.5)/NU);
50         y_i = Ylist(i-ii*NU)+ii*l1;
51         y_j = Ylist(j-jj*NU)+jj*l1;
52         x_i = Xlist(i-ii*NU);
53         x_j = Xlist(j-jj*NU);
54         %dx = dcell.alpha(1);
55         Alpha(i,j) = ...
                    Alpha(i,j)*exp(1i*q*(-Bz)*(y_i+y_j)/2*(x_i-x_j)/hbar*AtoM^2);
56     end
57 end
58
59 % Modify beta
60 for i = 1:NU*NW
61     for j = 1:NU*NW
62         ii = floor((i-0.5)/NU);
63         jj = floor((j-0.5)/NU);
64         y_i = Ylist(i-ii*NU)+ii*l1;
65         y_j = Ylist(j-jj*NU)+jj*l1;
66         x_i = Xlist(i-ii*NU);
67         x_j = Xlist(j-jj*NU);
68         %dx = dcell.beta1(1);

```

```

69         Beta(i,j) = Beta(i,j)*exp(1i*q*(-Bz)*(y_i+y_j)/2*(x_i-x_j+12)\|
70         /hbar*AtoM^2);
71     end
72 end
73
74 else
75
76     fprintf('using gauge2 \n');
77     % Modify alpha
78     for i = 1:NU*NW
79         for j = 1:NU*NW
80             ii = floor((i-0.5)/NU);
81             jj = floor((j-0.5)/NU);
82             y_i = Ylist(i-ii*NU);
83             y_j = Ylist(j-jj*NU);
84             x_i = Xlist(i-ii*NU)+ii*12;
85             x_j = Xlist(j-jj*NU)+jj*12;
86             %dy = dcell.alpha(2);
87             Alpha(i,j) = ...
89                 Alpha(i,j)*exp(1i*q*(-Bz)*(x_i+x_j)/2*(y_i-y_j)/hbar*AtoM^2);
88         end
89     end
90
91     % Modify beta
92     for i = 1:NU*NW
93         for j = 1:NU*NW
94             ii = floor((i-0.5)/NU);

```

```

95         jj = floor((j-0.5)/NU);
96         y_i = Ylist(i-ii*NU);
97         y_j = Ylist(j-jj*NU);
98         x_i = Xlist(i-ii*NU)+ii*12;
99         x_j = Xlist(j-jj*NU)+jj*12;
100        %dy = dcell_beta2(2);
101        Beta(i,j) = Beta(i,j)*exp(1i*q*(-Bz)*(x_i+x_j)/2*(y_i-y_j+11)\|
102        /hbar*AtoM^2);
103    end
104 end
105
106 end
107
108 % Hamiltonian:
109 H = kron(diag(ones(1,NL)),Alpha)+kron(diag(ones(1,NL- ...
110     1),1),Beta)+kron(diag(ones(1,NL-1),-1),Beta');

```

For non-equilibrium Green function transport calculation:

```

1 % Hamiltonian:
2 H = kron(diag(ones(1,NL)),Alpha)+kron(diag(ones(1,NL- ...
3     1),1),Beta)+kron(diag(ones(1,NL-1),-1),Beta');
4 %Define Energy grid for calculation of Transmission
5 E = linspace(-1,1,51);
6 %Define the matrices for NEGF
7 T = zeros(1,length(E));

```

```

8 green1 = inv(E(1)*eye(NW*NU)-Alpha);
9 green2 = inv(E(1)*eye(NW*NU)-Alpha);
10 Es = zeros(NT);
11 Esin = zeros(NT);
12 fprintf(1, 'Done\n');
13
14 %% NEGF Calculations
15 fprintf(1, 'Running NEGF...please wait\n')
16 fprintf(1, 'Energy range = %d eV to %d eV\n', min(E), max(E));
17 fprintf(1, '%s\n', ['[', blanks(length(E)), ']']);
18 fprintf(1, ' ');
19
20 %Run for each energy
21 for k = 1:length(E)
22 %Calculate surface GFs self consistently
23 %Calculate for beta'
24     err = 100;
25     while(err>errmax)
26         glnew = inv((E(k)+zplus)*eye(NW*NU)-Alpha-Beta'*green1*Beta);
27         err = (sum(sum(abs(glnew-green1))))/(sum(sum(abs(glnew+green1))));
28         green1 = glnew;
29     end
30     sigma1 = Beta'*green1*Beta;
31 %Calculate for beta
32     err = 100;
33     while(err>errmax)
34         g2new = inv((E(k)+zplus)*eye(NW*NU)-Alpha-Beta*green2*Beta');

```

```

35     err = (sum(sum(abs(g2new-green2)))) / (sum(sum(abs(g2new+green2))));
36     green2 = g2new;
37     end
38     sigma2 = Beta*green2*Beta';
39 %Calculate self energy matrices
40     E1 = kron(diag([1 zeros(1,NL-1)]),sigma1);
41     E2 = kron(diag([zeros(1,NL-1) 1]),sigma2);
42 %Calculate broadening
43     G1 = 1i*(E1-E1');
44     G2 = 1i*(E2-E2');
45 %Calculate G, Gn, A, T for coherent transport
46 %     G = inv((E(k)+1i*etaplus)*eye(NT)-H-E1-E2);
47 %     T(k) = real(trace(G1*G*G2*G'));
48 %     Gn = f1*(G*G1*G')+f2*(G*G2*G');
49 %     A = i*(G-G');
50 %Calculate G, Gn, A, T self consistently including the phase breaking ...
    processes
51     err = 100;
52     while(err>errmax)
53         G = inv((E(k)+zplus)*eye(NT)-H-E1-E2-Es);
54         Esnew = D*G;
55         err = sum(sum(abs(Esnew-Es))) / sum(sum(abs(Esnew+Es)));
56         Es = Esnew;
57     end
58
59 %     err = 100;
60 %     while(err>errmax)

```

```

61 %           Gn = f1*(G*G1*G')+f2*(G*G2*G')+(G*Esin*G');
62 %           Esinnew = D*Gn;
63 %           err = sum(sum(abs(Esinnew-Esin)))/sum(sum(abs(Esinnew+Esin))); ...
           Esin = Esinnew;
64 %           end
65 %           A=i*(G-G');
66           T(k) = real(trace(G1*G*G2*G'));
67           fprintf(1, '|');
68 end
69
70 fprintf(1, '\n');
71 fprintf(1, 'NEGF part Done\n');

```

Bibliography

- [1] K. Zhou, D. Wickramaratne, S. Ge, S. Su, A. De, and R. K. Lake, “Interlayer resistance of misoriented mos 2,” *Physical Chemistry Chemical Physics*, vol. 19, no. 16, pp. 10406–10412, 2017.
- [2] Y. Shi, S. Che, K. Zhou, S. Ge, Z. Pi, T. Espiritu, T. Taniguchi, K. Watanabe, Y. Barlas, R. Lake, *et al.*, “Tunable lifshitz transitions and multiband transport in tetralayer graphene,” *Physical review letters*, vol. 120, no. 9, p. 096802, 2018.
- [3] M. Serbyn and D. A. Abanin, “New dirac points and multiple landau level crossings in biased trilayer graphene,” *Physical Review B*, vol. 87, no. 11, p. 115422, 2013.
- [4] K. S. Novoselov, A. K. Geim, S. V. Morozov, D. Jiang, Y. Zhang, S. V. Dubonos, I. V. Grigorieva, and A. A. Firsov, “Electric field effect in atomically thin carbon films,” *science*, vol. 306, no. 5696, pp. 666–669, 2004.
- [5] Y. Zhang, Y.-W. Tan, H. L. Stormer, and P. Kim, “Experimental observation of the quantum hall effect and berry’s phase in graphene,” *nature*, vol. 438, no. 7065, p. 201, 2005.
- [6] A. C. Neto, F. Guinea, N. M. Peres, K. S. Novoselov, and A. K. Geim, “The electronic properties of graphene,” *Reviews of modern physics*, vol. 81, no. 1, p. 109, 2009.
- [7] M. Y. Han, B. Özyilmaz, Y. Zhang, and P. Kim, “Energy band-gap engineering of graphene nanoribbons,” *Physical review letters*, vol. 98, no. 20, p. 206805, 2007.
- [8] G. Gui, J. Li, and J. Zhong, “Band structure engineering of graphene by strain: first-principles calculations,” *Physical Review B*, vol. 78, no. 7, p. 075435, 2008.
- [9] B. Radisavljevic, A. Radenovic, J. Brivio, i. V. Giacometti, and A. Kis, “Single-layer mos 2 transistors,” *Nature nanotechnology*, vol. 6, no. 3, p. 147, 2011.
- [10] Z. Gong, G.-B. Liu, H. Yu, D. Xiao, X. Cui, X. Xu, and W. Yao, “Magnetoelectric effects and valley-controlled spin quantum gates in transition metal dichalcogenide bilayers,” *Nature communications*, vol. 4, p. 2053, 2013.

- [11] S. Wu, J. S. Ross, G.-B. Liu, G. Aivazian, A. Jones, Z. Fei, W. Zhu, D. Xiao, W. Yao, D. Cobden, *et al.*, “Electrical tuning of valley magnetic moment through symmetry control in bilayer mos 2,” *Nature Physics*, vol. 9, no. 3, p. 149, 2013.
- [12] A. M. Jones, H. Yu, J. S. Ross, P. Klement, N. J. Ghimire, J. Yan, D. G. Mandrus, W. Yao, and X. Xu, “Spin-layer locking effects in optical orientation of exciton spin in bilayer WSe₂,” *Nature Physics*, vol. 10, no. 2, pp. 130–134, 2014.
- [13] D. Wickramaratne, F. Zahid, and R. K. Lake, “Electronic and thermoelectric properties of few-layer transition metal dichalcogenides,” *The Journal of Chemical Physics*, vol. 140, no. 12, p. 124710, 2014.
- [14] R. Dhall, M. R. Neupane, D. Wickramaratne, M. Mecklenburg, Z. Li, C. Moore, R. K. Lake, and S. Cronin, “Direct bandgap transition in many-layer mos2 by plasma-induced layer decoupling,” *Advanced Materials*, vol. 27, no. 9, pp. 1573–1578, 2015.
- [15] A. Zhan, S. Colburn, R. Trivedi, T. K. Fryett, C. M. Dodson, and A. Majumdar, “Low-contrast dielectric metasurface optics,” *ACS Photonics*, vol. 3, no. 2, pp. 209–214, 2016.
- [16] C. Gong, H. Zhang, W. Wang, L. Colombo, R. M. Wallace, and K. Cho, “Band alignment of two-dimensional transition metal dichalcogenides: Application in tunnel field effect transistors,” *Applied Physics Letters*, vol. 103, no. 5, p. 053513, 2013.
- [17] H. Fang, C. Battaglia, C. Carraro, S. Nemsak, B. Ozdol, J. S. Kang, H. A. Bechtel, S. B. Desai, F. Kronast, A. A. Unal, *et al.*, “Strong interlayer coupling in van der waals heterostructures built from single-layer chalcogenides,” *Proceedings of the National Academy of Sciences*, vol. 111, no. 17, pp. 6198–6202, 2014.
- [18] A. F. Rigosi, H. M. Hill, Y. Li, A. Chernikov, and T. F. Heinz, “Probing interlayer interactions in transition metal dichalcogenide heterostructures by optical spectroscopy: Mos2/ws2 and mose2/wse2,” *Nano letters*, vol. 15, no. 8, pp. 5033–5038, 2015.
- [19] Y. Gong, S. Lei, G. Ye, B. Li, Y. He, K. Keyshar, X. Zhang, Q. Wang, J. Lou, Z. Liu, *et al.*, “Two-step growth of two-dimensional wse2/mose2 heterostructures,” *Nano letters*, vol. 15, no. 9, pp. 6135–6141, 2015.
- [20] C.-H. Lee, G.-H. Lee, A. M. Van Der Zande, W. Chen, Y. Li, M. Han, X. Cui, G. Arefe, C. Nuckolls, T. F. Heinz, *et al.*, “Atomically thin p–n junctions with van der waals heterointerfaces,” *Nature nanotechnology*, vol. 9, no. 9, p. 676, 2014.
- [21] K. Burke and friends, “The abc of dft,” *University Lecture*, 2007.
- [22] P. Hohenberg and W. Kohn, “Inhomogeneous electron gas,” *Physical review*, vol. 136, no. 3B, p. B864, 1964.
- [23] W. Kohn and L. J. Sham, “Self-consistent equations including exchange and correlation effects,” *Physical review*, vol. 140, no. 4A, p. A1133, 1965.

- [24] M. S. Dresselhaus and G. Dresselhaus, “Intercalation compounds of graphite,” *Advances in physics*, vol. 51, no. 1, pp. 1–186, 2002.
- [25] M. Koshino and E. McCann, “Parity and valley degeneracy in multilayer graphene,” *Physical Review B*, vol. 81, no. 11, p. 115315, 2010.
- [26] A. M. DaSilva, J. Jung, S. Adam, and A. H. MacDonald, “Transport and particle-hole asymmetry in graphene on boron nitride,” *Physical Review B*, vol. 91, no. 24, p. 245422, 2015.
- [27] K. Liu, L. Zhang, T. Cao, C. Jin, D. Qiu, Q. Zhou, A. Zettl, P. Yang, S. G. Louie, and F. Wang, “Evolution of interlayer coupling in twisted molybdenum disulfide bilayers,” *Nature communications*, vol. 5, no. 4966, p. 5966, 2014.
- [28] S. Huang, X. Ling, L. Liang, J. Kong, H. Terrones, V. Meunier, and M. S. Dresselhaus, “Probing the interlayer coupling of twisted bilayer mos2 using photoluminescence spectroscopy,” *Nano letters*, vol. 14, no. 10, pp. 5500–5508, 2014.
- [29] A. M. van der Zande, J. Kunstmann, A. Chernikov, D. A. Chenet, Y. You, X. Zhang, P. Y. Huang, T. C. Berkelbach, L. Wang, F. Zhang, M. S. Hybertsen, D. A. Muller, D. R. Reichman, T. F. Heinz, and J. C. Hone, “Tailoring the electronic structure in bilayer molybdenum disulfide via interlayer twist,” *Nano Letters*, vol. 14, no. 7, pp. 3869–3875, 2014.
- [30] C. H. Lui, Z. Ye, C. Ji, K.-C. Chiu, C.-T. Chou, T. I. Andersen, C. Means-Shively, H. Anderson, J.-M. Wu, T. Kidd, Y.-H. Lee, and R. He, “Observation of interlayer phonon modes in van der waals heterostructures,” *Phys. Rev. B*, vol. 91, p. 165403, Apr 2015.
- [31] P.-C. Yeh, W. Jin, N. Zaki, J. Kunstmann, D. A. Chenet, G. Arefe, J. T. Sadowski, J. I. Dadap, P. Sutter, J. C. Hone, and R. M. Osgood, Jr., “Direct measurement of the tunable electronic structure of bilayer mos2 by interlayer twist,” *Nano Letters*, vol. 16, no. 2, pp. 953–959, 2016.
- [32] H. Yu, Y. Wang, Q. Tong, X. Xu, and W. Yao, “Anomalous light cones and valley optical selection rules of interlayer excitons in twisted heterobilayers,” *Phys. Rev. Lett.*, vol. 115, no. 18, p. 187002, 2015.
- [33] P. Rivera, K. L. Seyler, H. Yu, J. R. Schaibley, J. Yan, D. G. Mandrus, W. Yao, and X. Xu, “Valley-polarized exciton dynamics in a 2d semiconductor heterostructure,” *Science*, vol. 351, no. 6274, pp. 688–691, 2016.
- [34] Y. Tan, F. Chen, and A. W. Ghosh, ‘First principles study and empirical parametrization of twisted bilayer MoS₂ based on band-folding,’ arXiv:1606.01858v1, June 6, 2016.
- [35] S. Shallcross, S. Sharma, E. Kandelaki, and O. Pankratov, “Electronic structure of turbostratic graphene,” *Physical Review B*, vol. 81, no. 16, p. 165105, 2010.

- [36] J. E. Padilha, H. Peelaers, A. Janotti, and C. G. V. de Walle, “Nature and evolution of the band-edge states in MoS₂: From monolayer to bulk,” *Phys. Rev. B*, vol. 90, no. 20, p. 205420, 2014.
- [37] R. Dhall, K. Seyler, Z. Li, D. Wickramaratne, M. R. Neupane, I. Chatzakis, E. Kosmowska, R. K. Lake, X. Xu, and S. B. Cronin, “Strong circularly polarized photoluminescence from multilayer mos2 through plasma driven direct-gap transition,” *ACS Photonics*, vol. 3, no. 3, pp. 310–314, 2016.
- [38] V. Perebeinos, J. Tersoff, and P. Avouris, “Phonon-mediated interlayer conductance in twisted graphene bilayers,” *Phys. Rev. Lett.*, vol. 109, no. 23, p. 236604, 2012.
- [39] D. Wickramaratne, ‘Electronic, Vibrational, and Thermoelectric Properties of Two-Dimensional Materials,’ Ph.D. Dissertation, University of California Riverside, 2015. Table A.2.
- [40] A. Kormányos, G. Burkard, M. Gmitra, J. Fabian, V. Zólyomi, N. D. Drummond, and V. Fal’ko, “k·p theory for two-dimensional transition metal dichalcogenide semiconductors,” *2D Materials*, vol. 2, no. 2, p. 022001, 2015.
- [41] H. Peelaers and C. G. Van de Walle, “Effects of strain on band structure and effective masses in MoS₂,” *Physical Review B*, vol. 86, no. 24, p. 241401, 2012.
- [42] Y. Meir and N. Wingreen, “Landauer formula for the current through an interacting electron region,” *Phys. Rev. Lett.*, vol. 68, p. 2512, 1992.
- [43] Z. Yu, Y. Pan, Y. Shen, Z. Wang, Z.-Y. Ong, T. Xu, R. Xin, L. Pan, B. Wang, L. Sun, *et al.*, “Towards intrinsic charge transport in monolayer molybdenum disulfide by defect and interface engineering,” *Nature communications*, vol. 5, 2014.
- [44] Z. Jin, X. Li, J. T. Mullen, and K. W. Kim, “Intrinsic transport properties of electrons and holes in monolayer transition-metal dichalcogenides,” *Physical Review B*, vol. 90, no. 4, p. 045422, 2014.
- [45] R. Bistritzer and A. H. MacDonald, “Transport between twisted graphene layers,” *Physical Review B*, vol. 81, no. 24, p. 245412, 2010.
- [46] K. M. M. Habib, S. S. Sylvia, S. Ge, M. Neupane, and R. K. Lake, “The coherent interlayer resistance of a single, rotated interface between two stacks of ab graphite,” *Appl. Phys. Lett.*, vol. 103, no. 24, p. 243114, 2013.
- [47] M. J. W. Rodwell, M. Le, and B. Brar, “Inp bipolar ics: Scaling roadmaps, frequency limits, manufacturable technologies,” *Proc. IEEE*, vol. 96, no. 2, pp. 271 – 286, 2008.
- [48] A. Avetisyan, B. Partoens, and F. Peeters, “Electric-field control of the band gap and fermi energy in graphene multilayers by top and back gates,” *Physical Review B*, vol. 80, no. 19, p. 195401, 2009.

- [49] K. S. Novoselov, A. K. Geim, S. Morozov, D. Jiang, M. Katsnelson, I. Grigorieva, S. Dubonos, Firsov, and AA, “Two-dimensional gas of massless dirac fermions in graphene,” *nature*, vol. 438, no. 7065, p. 197, 2005.
- [50] K. S. Novoselov, E. McCann, S. Morozov, V. I. Fal’ko, M. Katsnelson, U. Zeitler, D. Jiang, F. Schedin, and A. Geim, “Unconventional quantum hall effect and berry’s phase of 2π in bilayer graphene,” *Nature physics*, vol. 2, no. 3, p. 177, 2006.
- [51] Y. Shi, Y. Lee, S. Che, Z. Pi, T. Espiritu, P. Stepanov, D. Smirnov, C. N. Lau, and F. Zhang, “Energy gaps and layer polarization of integer and fractional quantum hall states in bilayer graphene,” *Physical review letters*, vol. 116, no. 5, p. 056601, 2016.
- [52] P. Stepanov, Y. Barlas, T. Espiritu, S. Che, K. Watanabe, T. Taniguchi, D. Smirnov, and C. N. Lau, “Tunable symmetries of integer and fractional quantum hall phases in heterostructures with multiple dirac bands,” *Physical review letters*, vol. 117, no. 7, p. 076807, 2016.
- [53] Y. Lee, J. Velasco Jr, D. Tran, F. Zhang, W. Bao, L. Jing, K. Myhro, D. Smirnov, and C. N. Lau, “Broken symmetry quantum hall states in dual-gated aba trilayer graphene,” *Nano letters*, vol. 13, no. 4, pp. 1627–1631, 2013.
- [54] J. Velasco Jr, L. Jing, W. Bao, Y. Lee, P. Kratz, V. Aji, M. Bockrath, C. Lau, C. Varma, R. Stillwell, *et al.*, “Transport spectroscopy of symmetry-broken insulating states in bilayer graphene,” *Nature Nanotechnology*, vol. 7, no. 3, p. 156, 2012.
- [55] E. McCann and V. I. Fal’ko, “Landau-level degeneracy and quantum hall effect in a graphite bilayer,” *Physical Review Letters*, vol. 96, no. 8, p. 086805, 2006.
- [56] E. McCann and M. Koshino, “The electronic properties of bilayer graphene,” *Reports on Progress in Physics*, vol. 76, no. 5, p. 056503, 2013.
- [57] A. Varlet, D. Bischoff, P. Simonet, K. Watanabe, T. Taniguchi, T. Ihn, K. Ensslin, M. Mucha-Kruczyński, and V. I. Fal’ko, “Anomalous sequence of quantum hall liquids revealing a tunable lifshitz transition in bilayer graphene,” *Physical review letters*, vol. 113, no. 11, p. 116602, 2014.
- [58] Y. Lemonik, I. Aleiner, C. Toke, and V. Fal’ko, “Spontaneous symmetry breaking and lifshitz transition in bilayer graphene,” *Physical review b*, vol. 82, no. 20, p. 201408, 2010.
- [59] Y. Barlas, “Counterpropagating fractional hall states in mirror-symmetric dirac semimetals,” *Physical review letters*, vol. 121, no. 6, p. 066602, 2018.
- [60] P. Stepanov, “Quantum parity hall effect in aba graphene.” Personal communication.
- [61] J. Velasco Jr, Y. Lee, Z. Zhao, L. Jing, P. Kratz, M. Bockrath, and C. Lau, “Transport measurement of landau level gaps in bilayer graphene with layer polarization control,” *Nano letters*, vol. 14, no. 3, pp. 1324–1328, 2014.

- [62] G. Kresse and J. Hafner, “Ab initio molecular dynamics for liquid metals,” *Phys. Rev. B*, vol. 47, pp. 558–561, Jan 1993.
- [63] G. Kresse and J. Furthmüller, “Efficiency of ab-initio total energy calculations for metals and semiconductors using a plane-wave basis set,” *Comput. Mater. Sci.*, vol. 6, no. 1, pp. 15–50, 1996.
- [64] G. Kresse and J. Furthmüller, “Efficient iterative schemes for ab initio total-energy calculations using a plane-wave basis set,” *Phys. Rev. B*, vol. 54, pp. 11169–11186, Oct 1996.
- [65] J. P. Perdew, K. Burke, and M. Ernzerhof, “Generalized Gradient Approximation Made Simple,” *Phys. Rev. Lett.*, vol. 77, pp. 3865–3868, 1996.
- [66] M. Ernzerhof and G. Scuseria, “Assessment of the perdew-burke-ernzerhof exchange-correlation functional,” *J. Chem. Phys.*, vol. 110, no. 11, pp. 5029–36, 1999.
- [67] S. Grimme, “Semiempirical gga-type density functional constructed with a long-range dispersion correction,” *Journal of Computational Chemistry*, vol. 27, no. 15, pp. 1787–1799, 2006.
- [68] K. Zhou, “<https://github.com/kzhoulatte>.” Private github.